2009

New design of switched reluctance motor using finite element analysis for hybrid electric vehicle applications

Anas Labak
University of Windsor

NEW DESIGN OF SWITCHED RELUCTANCE MOTOR USING FINITE ELEMENT ANALYSIS FOR HYBRID ELECTRIC VEHICLE APLLICATIONS

By

Anas Labak

A Thesis
Submitted to the Faculty of Graduate Studies
Through the Department of Electrical and Computer Engineering
in Partial Fulfillment of the Requirements for the
Degree of Master of Applied Science at the
University of Windsor

Windsor, Ontario, Canada

2009

Your file Votre référence
ISBN: 978-0-494-57633-5
Our file Notre référence
ISBN: 978-0-494-57633-5

AUTHOR'S DECLARATION OF ORIGINALITY

I hereby certify that I am the sole author of this thesis and that parts of this thesis have been published or submitted for publication. I also certify that I have the right to use all or part of the published work in other work.

I certify that, to the best of my knowledge, my thesis does not infringe upon anyone's copyright nor violate any proprietary rights and that any ideas, techniques, quotations, or any other material from the work of other people included in my thesis, published or otherwise, are fully acknowledged in accordance with the standard referencing practices.

I declare that this is a true copy of my thesis, including any final revisions, as approved by my thesis committee and the Graduate Studies office, and that this thesis has not been submitted for a higher degree to any other University or Institution.

ABSTRACT

Switched reluctance motors (SRMs) have been gaining increasing popularity and emerging as an attractive alternative to traditional electrical motors in hybrid vehicle applications due to their simple structure, ruggedness, ability of fault-tolerance, extremely high-speed operation, high power density, and low manufacturing cost. However, large torque ripple and acoustic noise are well-known as their major disadvantages.

This thesis presents a novel five-phase 15/12 SRM which features higher power density, very low level of vibration with flexibility in controlling the torque ripple profile. This design is classified as an axial field SRM, hence it needs 3-dimensional finite-element analysis model. Nonetheless, an alternative 2-dimensional model is developed and simulated using FEA software (MagNet) in order to analyze the proposed model.

The findings from the simulation is scrutinized and analyzed to realize various design features along with performance of the model. The finding in reference to the proposed axial field model is then compared with existing radial field models to validate its performance improvement. The manufacturing issues were addressed to prove its feasibility and cost effectiveness in conjunction with its assembly competences. Taking all the aspects into account superiority of new model's efficiency is comprehended to justify its application in HEV application.

DEDICATION

To My Family

ACKNOWLEDGEMENT

I am thankful to God Almighty for giving me the opportunity to pursue Masters program and the strength and patience to see it through. I am grateful to my wonderful parents whose love, encouragement and sacrifice has made me what I am today.

I wish to express my sincere gratitude to my advisor Dr. Narayan Kar for his assistance at every step of the way. His guidance has had an immense influence on my professional growth and without his technical expertise, reviews, and criticism it would not have been possible to shape this thesis. I would also like to thank my committee members Dr. Nader Zamani and Dr. Esam Abdel-Raheem for their valuable suggestions and guidance in the completion of this work.

In the end, I want to thank my fellow graduate students in the Electric Machines and Drives Research Lab for their support and encouragement. Working in their friendly company was a memorable experience.

TABLE OF CONTENTS

LIST OF FIGURES

LIST OF TABLES

NOMENCLATURE

Generally symbols have been defined locally. The list of principle symbols is given below.

A_s	Electric loading
A_{sp}	Stator pole area
B	Magnetic loading, magnetic flux density
B_c	Magnetic flux density in the core
B_g	Magnetic flux density in the air gap
B_s	Maximum magnetic flux density in the core
D	Bore diameter
F	MMF per phase
F_c	MMF drops in c-core stator
F_g	MMF drops in the air gap
F_r	MMF drops in the rotor cube
g	Air gap length
i	Instantaneous phase current
I	Current
I_r	Rated current
i_s	Saturation current
K_u	Constant relates the inductance ratio
k_d	Duty cycle constant
k_e	Efficiency constant
L	Winding inductance
L_a	Aligned inductance

L_a^u	Aligned unsaturated inductance
L_u	Unaligned unsaturated inductance
l_c	Flux path length in the core and rotor cube
L_u	Unaligned inductance
m	Number of phases
N	Number of turns per phase
N_r	Rotor speed (rpm)
P_d	Output power
P_r	Number of rotor poles
P_s	Number of stator poles
R	Phase resistance
r	Radius of the centre of a rotor cube
R_{ph}	Motor phase resistance
T	Torque
T_{av}	Average torque
$T_{Instmax}$	Maximum Instantaneous torque
$T_{Instmin}$	Minimum Instantaneous torque
TR	Torque ripple
t_r	Rotor-cube line length
V_s	Voltage of the source
W_{co}	Coenergy
W_e	Electric energy
W_f	Stored field energy
W_{fc}	field energy in the coil
W_m	Mechanical work

α	Ratio of the of inductances
β_r	Rotor pole arc
β_s	Stator pole arc
ε	Step size
λ	Unsaturated inductance ratio
μ	Magnetic permeability of the core material
μ_0	Magnetic permeability of the free space
θ	Angular rotor position
ω_m	Motor angular speed
τ_r	Rotor pole pitch
τ_s	Stator pole pitch
ψ	Flux linkage

1 INTRODUCTION

1.1 Overview

We live in a world of limited resources. In a world in such, one of the most precious resources is the environment in itself. If we look back into the last century, extreme emission of fossil fuel has pushed the world environment more and more towards impairment. This has been of a serious concern for quite a while now. Now with the Fossil fuel price on the rise along with the hunger added of fossil fuel the world economy is also facing climactic challenges.

Modern civilization owes its achievements to transportation system profoundly. Intensive growth of transportation is accompanied with rapid urbanization and industrialization, predominantly in developing country. At the same time as its price transportation is one of the highest patron of fossil fuel, consequently the largest contributor towards green house gas emission. In 1971, the global consumption of petroleum was close to 49 million barrels per day, 33 percent of which was consumed by transportation sector. This share increased to 48 percent of the 77 million barrels per day consumed in 2002. According to an estimate by the International Energy Annual, the global oil demand will spike up to 121 million barrels per day by 2030, 54 percent of which will be consumed by transportation alone.

Most of the transportation in use today has fossil fuel drive internal combustion engine (ICE) in use. Hybrid electric vehicles are designed with an objective to reduce both environmental hazard and dependence on fossil fuel. In a hybrid electric vehicle an electric motor is put together with an ICE to overcome many weakness of combustion engine as well as utilize the strength of electric motor in a vehicle.

1.2 History of Hybrid Electric Vehicles

1.2.1 Beginning

In 1901, while employed at Lohner Coach Factory, Ferdinand Porsche designed the Mixte, a 4WD series-hybrid version of "System Lohner-Porsche" electric carriage previously appeared in 1900 Paris Salon. The Mixte broke several Austrian speed records, and also won the Exelberg Rally in 1901. The Mixte used a gasoline engine powering a generator, which in turn powered electric hub motors, with a small battery pack for reliability. It had a range of 50 km, a top speed of 50 km/h and a power of 5.22 kW during 20 minutes.

In 1905, H. Piper filed a US patent application for a hybrid vehicle. [1] The 1915 Dual Power, made by the Woods Motor Vehicle electric car maker, had a four-cylinder ICE and an electric motor. Below 15 mph (25 km/h) the electric motor alone drove the vehicle, drawing power from a battery pack, and above this speed the "main" engine cut in to take the car up to its 35 mph (55 km/h) top speed. About 600 were made up to 1918.[2]

In 1931 Erich Gaichen invented and drove from Altenburg to Berlin a 1/2 horsepower electric car containing features later incorporated into hybrid cars with maximum speed 40 km/h. The car battery was re-charged by the motor when the car went downhill. Additional power to charge the battery was provided by a cylinder of compressed air which was re-charged by small air pumps activated by vibrations of the chassis and the brakes and by igniting oxyhydrogen gas. No production beyond the prototype was reported.

1.2.2 Predecessors of Current Technology

A more recent working prototype of the HEV was built by Victor Wouk. Wouk's work with HEVs in the 1960s and 1970s earned him the title as the "Godfather of the Hybrid". Wouk installed a prototype hybrid drivetrain (with a 16 kW electric motor) into

a 1972 Buick Skylark provided by GM for the 1970 Federal Clean Car Incentive Program.

The regenerative braking system, the core design concept of most production HEVs, was developed by electrical engineer David Arthurs around 1978 using off-the shelf components and an Opel GT. The vehicle exhibited 75 miles per US gallon (3.1 L/100 km; 90 mpg-imp) fuel efficiency.

In 1989, Audi produced its first iteration of the Audi Duo (or Audi 100 Avant duo) experimental vehicle, a plug-in parallel hybrid based on the Audi 100 Avant quattro. This car had a 12.6 bhp Siemens electric motor which drove the rear wheels. A trunk-mounted nickel-cadmium battery supplied energy to the motor that drove the rear wheels. The vehicle's front wheels were powered by a 2.3-litre five-cylinder engine with an output of 136 bhp (101 kW). The intent was to produce a vehicle which could operate on the engine in the country and electric mode in the city. Mode of operation could be selected by the driver. One drawback was that due to the extra weight of the electric drive, the vehicles were less efficient when running on their engines alone than standard Audi 100s with the same engine.

Two years later, Audi, unveiled the second duo generation - likewise based on the Audi 100 Avant quattro. Once again this featured an electric motor, a 28.6 bhp (21.3 kW) three-phase machine, driving the rear wheels. This time, however, the rear wheels were additionally powered via the Torsen differential from the main engine compartment, which housed a 2.0-litre four-cylinder engine.

1.2.3 Production HEVs

Automotive hybrid technology became successful in the 1990s when the Honda Insight and Toyota Prius became available. These vehicles have a mechanical linkage from the ICE to the driven wheels, so that some power is transferred from the engine to the wheels without conversion to and from electric energy.

The Prius has been in high demand since 2004. Newer designs have more conventional appearance and are less expensive, often appearing and performing

identically to their non-hybrid counterparts while delivering 40% better fuel efficiency. The Honda Civic Hybrid appears identical to the non-hybrid version, for instance, but delivers better mileage. The redesigned 2004 Toyota Prius improved passenger room, cargo area, and power output, while increasing energy efficiency and reducing emissions. The Honda Insight, while not matching the demand of the Prius, stopped being produced after 2006 and has a devoted base of owners. In 2004, Honda also released a hybrid version of the Accord but discontinued it in 2007 citing disappointing sales.

Honda, which offers Insight, Civic and Accord models, sold 26,773 HEVs in the first 11 months of 2004. Toyota had sold a cumulative 306,862 HEVs between 1997 and November 2004, and Honda had sold a total of 81,867 HEVs between 1999 and November 2004.

Audi was the first European car manufacturer to put in 1997 a hybrid vehicle into series production, the third generation Audi duo, then based on the A4 Avant.

2005 saw the first hybrid electric sport utility vehicle (SUV) released, the Ford Escape Hybrid. Toyota and Ford entered into a licensing agreement in March 2004 allowing Ford to use 20 patents from Toyota related to hybrid technology. Toyota announced calendar year 2005 hybrid electric versions of the Toyota Highlander and Lexus RX 400h with 4WD-i, which uses a rear electric motor to power the rear wheels negating the need for a differential. Toyota also plans to add hybrid drivetrains to ten new hybrid models by 2012 and expects to sell worldwide one million hybrids per year early in the coming decade.

In 2007, Lexus released a hybrid electric version of their GS sport sedan dubbed the GS450h with a power output of 335bhp. The 2007 Camry Hybrid became available in summer 2006 in the United States and Canada. Nissan announced the release of the Altima hybrid in 2007.

Commencing in 2008 General Motors began to market their 2-Mode Hybrid models of their GMT900 based Chevrolet Tahoe and GMC Yukon SUVs.

The Toyota hybrids combined with Lexus reached 1 million hybrids sold in the US by February 2009, and worldwide sales of hybrids by both carmakers reached over

1.7 million vehicles by January 2009. As a top seller in the US market, the Toyota Prius made up more than half of the 1.2 million Prius sold worldwide by early 2009.

The Ford Fusion Hybrid officially debuted at the Greater Los Angeles Auto Show in November 2008, and was launched to the U.S. market in March 2009, together with the second generation Honda Insight and the Mercury Milan Hybrid.

1.2.4 Pre-production HEVs

For the 2009 model year, the same technology will be offered in the Cadillac Escalade and their 1/2-ton pickup truck models, the 2009 Chevrolet Silverado and GMC Sierra 2-mode hybrid models. Also in 2009 GM's Saturn division is releasing the first front wheel drive version of the 2-mode technology with the appearance of the 2009 Saturn Vue 2-mode hybrid model.

Hyundai Motor Company plans to start retail sales of its first LPG–electric hybrid vehicle in July 2009. To be sold initially in the South Korean domestic market under the Avante badge, the Elantra LPI Hybrid Electric Vehicle (HEV) is the world's first hybrid vehicle to be powered by liquid petroleum gas (LPG) and the first to adopt advanced Lithium Polymer (Li–Poly) batteries.

Comparing operating costs among different types of hybrid vehicles currently available in the marketplace, the Elantra LPI HEV promises to be the cheapest of all to run. The Elantra LPI HEV promises to be as much as 40 percent cheaper to operate than other competitor models in the marketplace.

Honda will release the CR-Z in hybrid form in Feb 2010 in Japan.

1.3 Environmental Issues of Hybrid Electric Vehicles

1.3.1 Fuel Consumption

Current HEVs reduce fossil fuel consumption under certain circumstances, compared to otherwise similar conventional vehicles, primarily by using three mechanisms [3]:

- Decrease consumption of energy during idle/low output,
- usually by turning the ICE off
- Recapture wasted energy (i.e. regenerative braking)
- Reduce the size and power of the ICE, and hence inefficiencies from under-utilization, by using the added power from the electric motor to compensate for the loss in peak power output from the smaller ICE.

Any combination of these three primary hybrid advantages may be used in different vehicles to realize different fuel usage, power, emissions, weight and cost profiles. The ICE in an HEV can be smaller, lighter, and more efficient than the one in a conventional vehicle, because the combustion engine can be sized for slightly above average power demand rather than peak power demand. The drive system in a vehicle is required to operate over a range of speed and power, but an ICE's highest efficiency is in a narrow range of operation, making conventional vehicles inefficient. On the contrary, in most HEV designs, the ICE operates closer to its range of highest efficiency more frequently. The power curve of electric motors is better suited to variable speeds and can provide substantially greater torque at low speeds compared with internal-combustion engines. The greater fuel economy of HEVs has implication for reduced petroleum consumption and vehicle air pollution emissions worldwide.

1.3.2 Noise

Reduced noise emissions resulting from substantial use of the electric motor at idling and low speeds, leading to roadway noise reduction, [4] in comparison to conventional gasoline or diesel powered engine vehicles, resulting in beneficial noise health effects (although road noise from tires and wind, the loudest noises at highway speeds from the interior of most vehicles, are not affected by the hybrid design alone).

Reduced noise may not be beneficial for all road users, as blind people or the visually-impaired consider the noise of combustion engines a helpful aid while crossing streets and feel quiet hybrids could pose an unexpected hazard. The U.S. Congress and the European Commission are exploring legislation to establish a minimum level of sound

for electric and hybrid electric vehicles when operating in electric mode, so that blind people and other pedestrians and cyclists can hear them coming and detect from which direction they are approaching. Tests have shown that vehicles operating in electric mode can be particularly hard to hear below 20 mph (32 km/h).

1.3.3 Pollution

Reduced air pollution emissions, due to lower fuel consumption, lead improved human health with regard to respiratory problems and other illnesses. Pollution reduction in urban environments may be particularly significant due to elimination of idle-at-rest.

Battery toxicity is a concern, although today's hybrids use NiMH batteries, not the environmentally problematic rechargeable nickel cadmium. "Nickel metal hydride batteries are benign. They can be fully recycled," says Ron Cogan, editor of the Green Car Journal. Toyota and Honda say that they will recycle dead batteries and that disposal will pose no toxic hazards. Toyota puts a phone number on each battery, and they pay a $200 "bounty" for each battery to help ensure that it will be properly recycled.

Hybrid Vehicle emissions today are getting close to or even lower than the recommended level set by the EPA (Environmental Protection Agency). The recommended levels they suggest for a typical passenger vehicle should be equated to 5.5 metric tons of carbon dioxide. The three most popular hybrid vehicles, Honda Civic, Honda Insight and Toyota Prius, set the standards even higher by producing 4.1, 3.5, and 3.5 tons showing a major improvement in carbon dioxide emissions.

1.4 Electric Motors

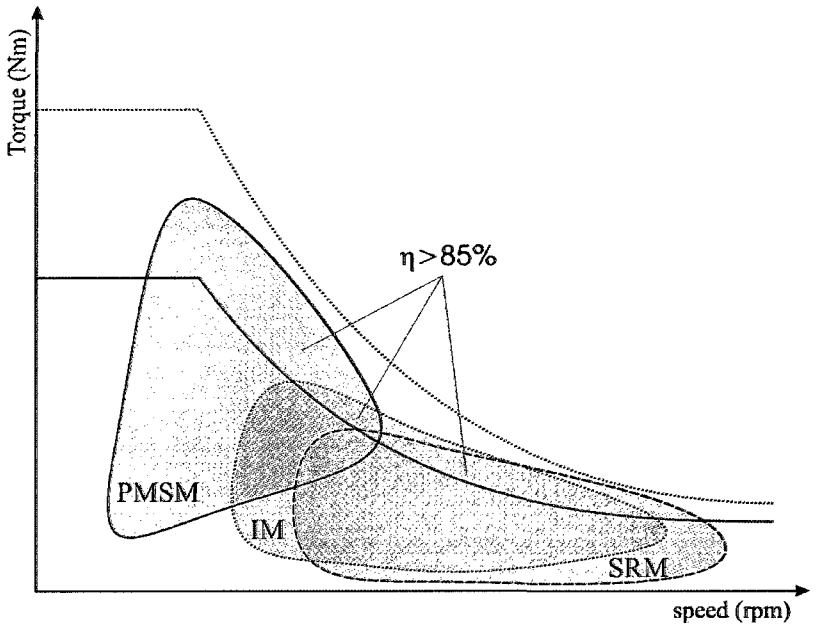

Figure 1.1. Torque speed characteristics of (IMs), (PMSMs) and (SRMs).

Performance of an HEV relies on the design and control of its electric propulsion system that consists of a traction motor, its power electronic drive, motor controller and an energy storage element such as battery. HEV propulsion requires high instant power and power density, wide speed ranges in constant torque and constant power operation, high efficiency and reliability. Selection of a suitable electric motor to fulfill these requirements continues to pose a challenge [6]. Several motors have been analyzed for traction purposes [7]-[13] amongst which direct current motor (DCMs), induction motors (IMs), permanent magnet synchronous motors (PMSMs) and switched reluctance motors (SRMs) are considered the most fitting candidates.

1.4.1 DC Motors (DCs)

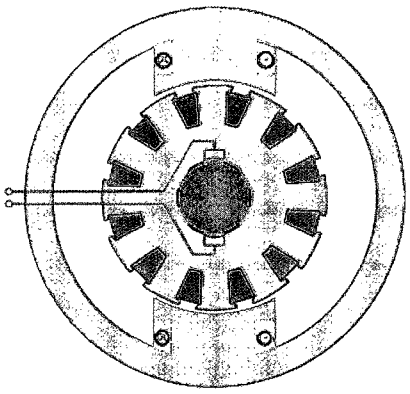

Figure 1.2. DC motor.

Torque–speed characteristics of DC motor in addition to simpler speed control is proved to be gratifying in electric propulsion when it comes to the traction requirement. On the down side DC motor drives have a bulky construction, low efficiency, low reliability, and higher need of maintenance, mainly due to the presence of the mechanical commutators, even though with some progress with slippery contacts. Moreover, in traction applications the advancement of rugged solid-state power semiconductors made it gradually more realistic to introduce AC induction and synchronous motor drives. However, with consideration to the cost of the inverter, ac drives are used generally just for higher power. At low power ratings, the dc motor is still an attractive choice. Improvement of existing vehicle systems without changing the mechanical part can be achieved by the new DC chopper power electronics. On this context it worth mentioning a French automaker PSA Peugeot Citroën, who introduced the HEV version of the well-known Berlingo, which is called Dynavolt, with a dc motor as electric propulsion [4].

1.4.2 Induction Motors(IMs)

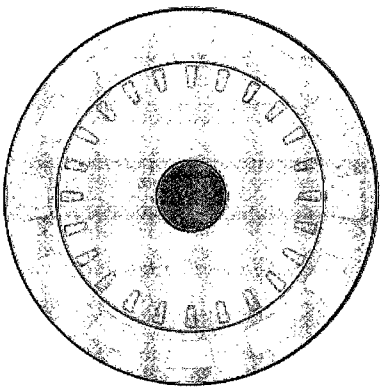

Figure 1.3. Induction motor(IM).

Dependability, low cost and wide speed ranges at constant power has made induction motors a appropriate choice in context to HEVs. One major drawback is lower efficiency of induction motor in traction application for which several optimal flux control and energy optimization techniques are revolutionizing [14] – [18]. Modifications at the design level and fault tolerant, high performance control techniques are has made induction machine a more appropriate choice for induction motor [19] – [26].

Squirrel cage induction motors are most preferable choice for the electric propulsion of HEVs for their reliability, ruggedness, low maintenance, low cost, and ability to operate in hostile environments.

Primitively, a number of shortcomings of induction motor drive which undermined its use in HEVs were mainly high loss, low efficiency, low power factor, and low inverter-usage factor, which is more serious for the high speed, large power motor. One most critical problem was posed by its presence of breakdown torque limits when in extended constant-power operation where at critical speed the breakdown torque is reached.

Fortunately, these drawbacks are taken into consideration and being surmounted by more refined design along with the use of modern power electronics. [18]–[20]. The use of a multiphase pole-changing IM drive, especially for traction application, has been proven effective [26], [27].

1.4.3 Permanent Magnet Synchronous Motors (PMSMs)

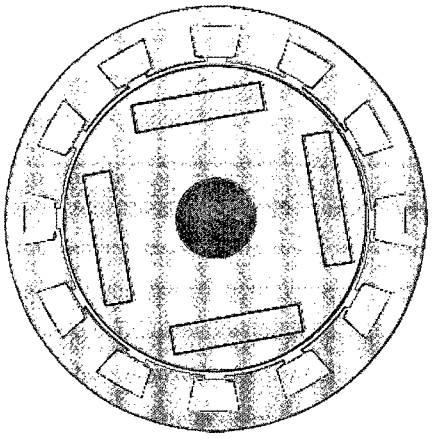

Figure 1.4. Permanent magnet synchronous motor(PMSM).

Permanent magnet synchronous motor is an admirable choice in the case of HEV propulsion system due to their higher efficiency, higher power density and lower weight. Inventive design and control technology are presently being investigated to overcome its weakness of field weakening capability to achieve optimal speed range in constant power region. Progress of robust, control strategies to achieve power output and torque response desired in traction application is also under persuasion [33] – [37].

Buried-magnet mounted permanent magnet motors are acknowledged for their ruggedness with higher air-gap flux density while the surface-mounted permanent magnet ones have an advantage of having less number of permanent magnets. An additional configuration is the so-called PM hybrid motor, where the air-gap magnetic field is obtained through the combination of PM and field winding. In the broader term, PM hybrid motor may also include the motor whose configuration utilize the combination of PM motor and reluctance motor. PM hybrid motors offer a wider speed range and a higher overall efficiency but with a more complex construction [5].

Finally, the PM brushless motor is particularly privileged and suited for the wheel direct-drive motor applications [33].

1.4.4 Switched Reluctance Motors (SRMs)

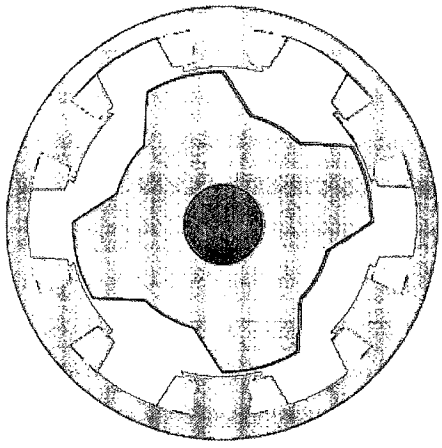

Figure 1.5. Switched reluctance motor.

Due their simple and rugged construction, high speed operation and extended constant power range, SRMs are gaining interest as a potential alternative in HEV traction [38] - [40]. However torque ripple and acoustic noise are major concerns in SRM drive performance. Research is currently focused towards analysis, design improvement and development of excitation schemes and control strategies to reduce these effects [41] - [45]. With the advancement in power electronics technology, new converter and motor drive topologies are also being introduced for improved performance and reduced losses for these motors [46] – [53].

SRMs are subjected to a great deal of curiosity and appreciation to have an impending prospect for HEV applications. They have several advantages which makes them this attractive; such as:

- simple and rugged construction
- fault-tolerant operation
- simple control
- outstanding torque–speed characteristics

On addition, extremely long constant-power range is one of the strengths.

Although there are several disadvantages; such as:

- Acoustic noise generation
- Torque ripple
- Special converter topology
- Excessive bus current ripple
- Electromagnetic-interference (EMI) noise generation.

Both the advantages and the disadvantages are significant for HEV applications. Acceptable solutions to the above disadvantages are needed to get a viable SRM-based HEV [33], [34]. Nonetheless, SRM can actually envisage potential solution for light and heavy HEV applications [35], [36].

1.5 Research Objective

The objective of this research is to overcome the major disadvantages of SRM in application of HEVs; with that purpose in mind a new design topology of SRM is proposed which is capable of delivering an SRM for the purpose of HEV application with extended driving range as well as wider speed range.

To achieve its purpose the new design is capable of delivering:

- Reducing torque ripple as well as acoustic noise using smaller flux paths by using axial flux path instead of radial flux path through the rotor.
- Enriching motor efficiency by means of having lower core losses in both stator and rotor.
- Increasing motor life as a consequence of have axial flux path.
- Exceptional design with C-core windings perturbed out of the stator in such a way so that significant improvement is accomplished in heat dissipation technique.
- Innovative design with significantly increased power density which is vital in application to HEVs.

- Design topology enabling more efficiency in manufacturing and maintenance as a result, lower cost manufacturing with low maintenance due to flexible and unique design of perturbed C-core model.

For the purpose the machine model is designed and consequently analyzed using FEA simulation software (MagNet).

1.6 Thesis Outline

This thesis is organized as follows:

Chapter 2: In this chapter, the background of switched reluctance machine is being scrutinized. To furnish a clear understanding, classification and basic design topology of SRM is looked into. To have a better perceptive the motor energy conversion and torque production fundamentals are conferred. Depicting motor operation and analyzing machine characteristics the machine mathematical model is also discussed in this chapter. Different machine drive topologies in machine control applications are also being scrutinized.

Chapter 3: This chapter is all about the design of proposed machine model. It describes different key features of the new design and details about specific design specifications

Chapter 4: In this chapter, the step by step design procedures of the new machine model are presented. The machine parameters are optimized. In order to predict the machine power rating, the output power equation is derived according to its special geometry.

Chapter 5: The designed model analyzed using FEA software (MagNet). To achieve this, the 3-D model of the machine is perceived in 2-D. The FEA results are used to represent the new machine performance. To validate these results, the model is compared against a standard machine performance.

Chapter 6: In this chapter, the manufacturing details and assembly issues of the proposed model is being looked into. In regards to this, different manufacturing challenges and tactical details are being examined along with the assembly steps.

Chapter 7: Findings of this research are summarized in this section.

2 FUNDAMENTALS OF SWITCHED RELUCTANCE MACHINES

2.1 Definition

Switched reluctance motor is a type of synchronous electric motor except of having salient poles both on the rotor and the stator along with concentrated set of coils each of which is wound on one pole and the exciting current commutation from one phase to the other is done electronically.

Torque is generated through the phenomenon of reluctance force in which the moveable part tends to move towards the position where the inductance of the excited winding is maximized; in other words where the reluctance of the excited phase is minimized. In a switched reluctant motor, motion may be rotary or linear. From structural stand point, rotor may be interior (as in Figure 2.1) or exterior. Generally the moveable part is a simple component made of soft magnetic iron, shaped in such a way as to maximize the variation of inductance with position. The geometrical simplicity is one of the main attractive features: since no windings or permanent magnets are used, the manufacturing cost appears to be lower than for other types of motor, while the reliability and robustness appear to be improved [54].

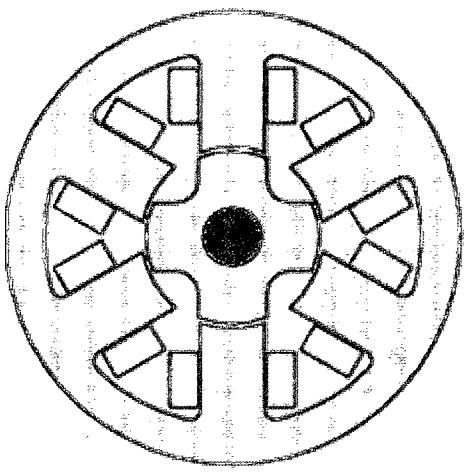

Figure 2.1. Switched reluctance motor.

2.2 History of the Switched Reluctance Motor

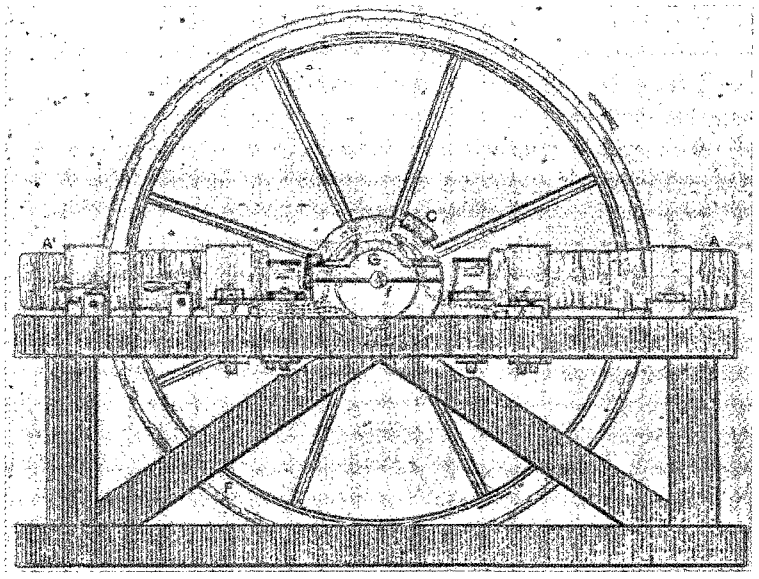

Figure 2.2. Davidson's electric motor.

The earliest recorded switched reluctance motor was the one built by Davison in Scotland in 1838 and used to propel a locomotive on the Glasgow-Edinburgh railway near Falkirk. The stepper motor that includes some of the features of the modern switched reluctance motor was invented and patented in the 1920's in Aberdeen by C.L. Walker. In 1969, S.A. Nasar introduced the basic concepts of the modern day switched reluctance machine [55]. The period of the late 70s was a time of development of concepts of the switched reluctance motor that was helped along with the development of fast switching devices culminating in the work by [56] and [57]. Since then there have been massive developments in the both the design and control of switched reluctance motors. [58].

2.3 SRM Configurations

Switched reluctance motors are primarily classified into two main categories; rotary switched reluctance motors (SRM) and Linear switched reluctance motors (LSRM)

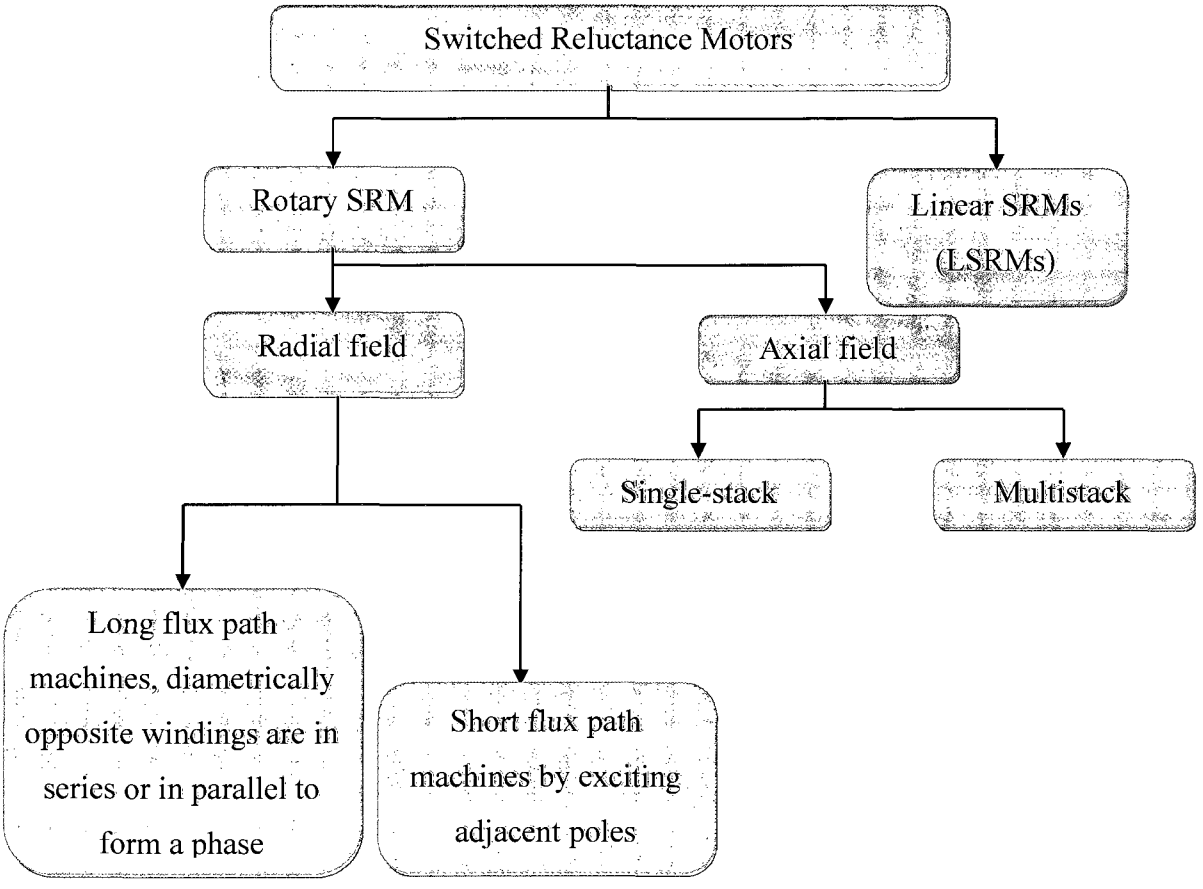

Figure 2.3. Classification of switched reluctance motor.

and that is done on the basis of the nature of the motion. The rotary SRMs are further differentiated by the orientation of the magnetic field path with respect to the axis of their shafts. If the magnetic field path is perpendicular to the shaft, which may also be seen as along the radius of the cylindrical stator and rotor, the SRM is classified as radial field. When the flux path is along the axial direction, the machine is called an axial field SRM.

Radial field SRMs are most commonly used. They can be divided into shorter and longer flux paths based on how a phase coil is placed. The conventional one is the long flux path SRMs, in which the phase coil is placed in the diametrically opposite slots. Short flux path SRMs have the advantage of lower core losses due to the fact that the flux reversals do not occur in stator back iron. They are ideal for applications where the total length may be constrained, such as in a ceiling fan or in a propulsion application. The

disadvantage of this configuration is that the stator laminations have to be folded one on top of the other, unlike the simple stacking of laminations in the radial field configuration.

The variety of combinations of number of phases with stator and rotor number and shapes of poles led to a wide range of possible designs of the SRM. There are various configurations of SRM designs which were proposed to improve the overall performance of the machine, e.g. a c-core stator was proposed in [59] as shown in Figure 2.5 to increase torque capability and efficiency and also to provide a higher flexibility in winding design.

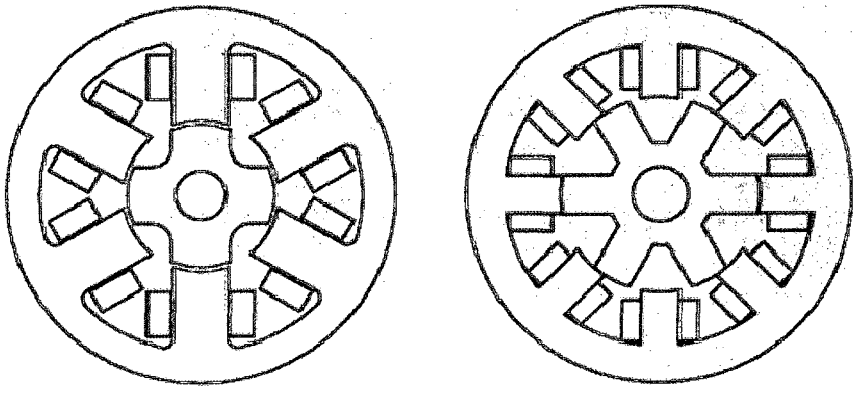

(a) (b)

Figure 2.4. Switched reluctance motor (a) 6/4 pole and (b) 8/6 pole.

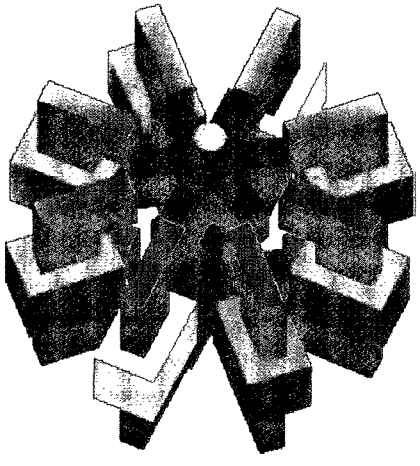

Figure 2.5. 3-D view of dual rotor configuration C-core switched reluctance motor.

2.4 Operation of the Switched Reluctance Motor

The reluctance motor is a type of synchronous machine. It has wound field coils of a DC motor for its stator windings and has no coils or magnets on its rotor. Fig. 2.1 shows its typical structure. It can be seen that both the stator and rotor have salient poles; hence, the machine is a doubly salient machine.

The rotor is aligned whenever the diametrically opposite stator poles are excited. In a magnetic circuit, the rotating part prefers to come to the minimum reluctance position at the instance of excitation. While two rotor poles are aligned to the two stator poles, another set of rotor poles is out of alignment with respect to a different set of stator poles. Then, this set of stator poles is excited to bring the rotor poles into alignment. This elementary operation can be explained by Fig.2.6 [60]. In the figure, consider that the rotor poles r1 and r1′ and stator poles c and c′ are aligned. Apply a current to phase a with the current direction as shown in Fig.2.6.a. A flux is established through stator poles a and a′ and rotor poles r2 and r2′ which tends to pull the rotor poles r2 and r2′ toward the stator poles a and a′, respectively. When they are aligned, the stator current of phase a is turned off and the corresponding situation is shown in Fig.2.6.b. Now the stator winding b is excited, pulling r1 and r1′ toward b and b′, respectively, in a clockwise direction. Likewise, energizing phase c winding results in the alignment of r2 and r2′ with c and c′, respectively. Accordingly, by switching the stator currents in such a sequence, the rotor is rotated. Similarly, the switching of current in the sequence of acb will result in the reversal of rotor rotation. Since the movement of the rotor, hence the production of torque and power, involves a switching of currents into stator windings when there is a variation of reluctance, this variable speed motor is referred to as a switched reluctance motor (SRM).

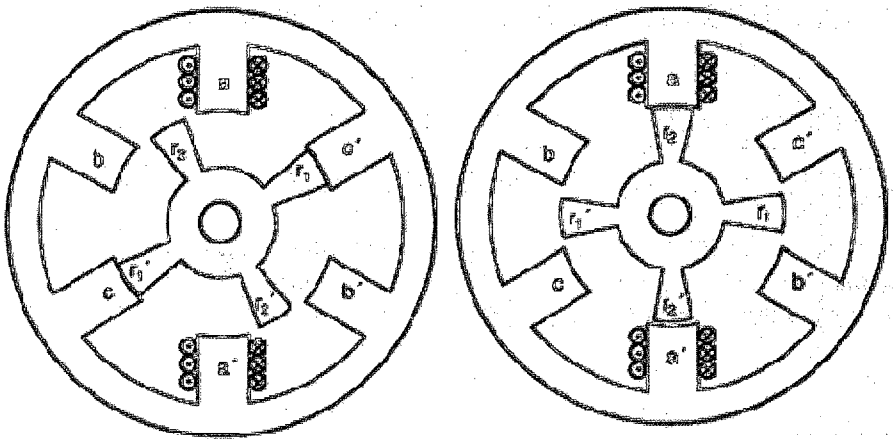

(a) (b)

Figure 2.6. Operation of SRM (a) phase c aligned and (b) phase a aligned.

2.5 Mathematical Model for SRM

During motor operation, each phase is excited when its inductance is increasing and unexcited when its inductance is decreasing Neglecting the mutual inductance, an equivalent circuit of the SRM could be derived from the voltage equation for one phase that is giving as follows

$$V = R_{ph} i + \frac{d\psi(\theta, i)}{dt} \tag{2.1}$$

It is basically the instant voltage across the terminals of a single phase of a SRM winding. This voltage is equal to the sum of the resistive voltage drop and the rate of the flux linkages, where, V is the terminal voltage, i is the phase current, R_{ph} is the motor phase resistance, and ψ is the flux linkage of the winding, which is function of the rotor position, and the motor current i,

$$\psi = L(\theta, i) \cdot i \tag{2.2}$$

where L is the winding inductance which is a function of the rotor position and excitation current.

By substituting (2.2) into (2.1) we get:

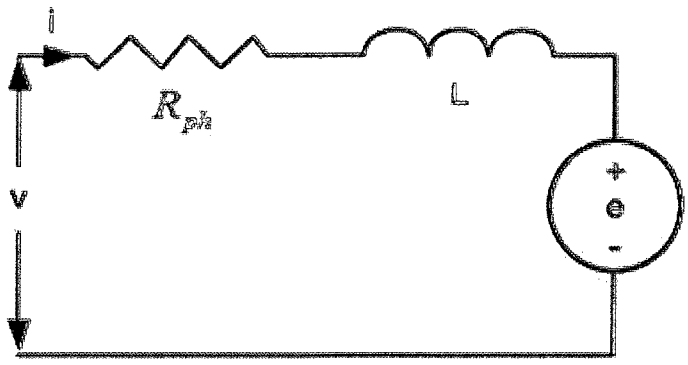

Figure 2.7. Equivalent circuit diagram of SRM.

$$V = R_{ph}i + L(\theta,i)\frac{di}{dt} + i\frac{d\theta}{dt}\cdot\frac{dL(\theta,i)}{d\theta} \tag{2.3}$$

$$V = R_{ph}i + L(\theta,i)\frac{di}{dt} + \frac{dL(\theta,i)}{d\theta}\cdot\omega_m \cdot i \tag{2.4}$$

In equation (2.4), the three terms on the right hand side represent the resistive voltage drop, the inductive voltage drop, and the induced emf, respectively. And hence the mathematical model is represented by the equivalent circuit shown in Fig.(2.7) [60]

2.6 Energy Conversion of the Switched Reluctance Motor

Electromechanical energy conversion analysis for SRM is necessary to explain the torque production physics (mechanism).

Multiplying both sides of the voltage equation (2.1) by *i*, gives an expression for the instantaneous power for SRM, [58]

$$Vi = R_{ph}i^2 + i\frac{d\psi(\theta,i)}{dt} \tag{2.5}$$

It can be seen from (2.5) that the power given to an SRM has two forms. The first term on the right hand side is the resistive load while the second term can be further expanded as follows; it can be explained from the energy conversion definition for SRM that is illustrated in the figures (2.8-2.13).

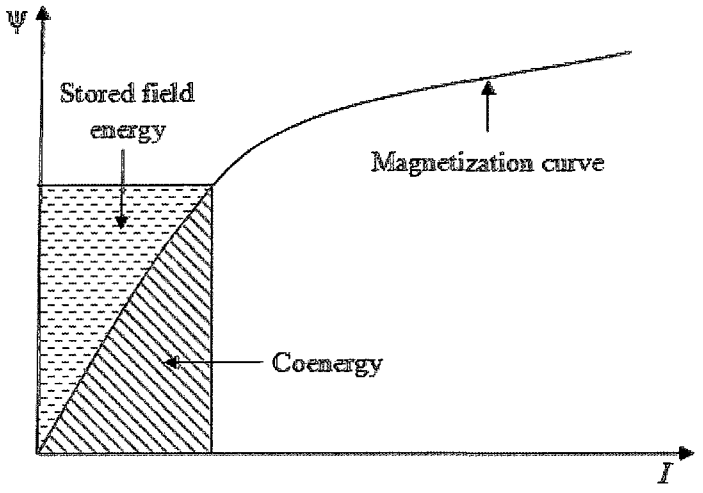

Figure 2.8. Electric energy division of SRM.

The electrical energy supplied from the voltage source at any moment is the sum of the coenergy and the stored field energy at this moment, as shown in fig (2.8)

The general expression for the torque produced is defined as

$$T = \left[\frac{\partial W_{co}}{\partial \theta}\right]_{i=const.} \tag{2.6}$$

where W_{co} is the coenergy, θ is the angular rotor position. At any position the coenergy is the area under the magnetization curve so it can be defined as follows

$$W_{co} = \int_0^{i_1} \psi di \tag{2.7}$$

where ψ is the flux linkage at any rotor position as a function of the current.

From (2.6) and (2.7), we can graphically demonstrate the instantaneous torque as the work ΔW_m divided by $\Delta\theta$ as illustrated in fig (2.9).

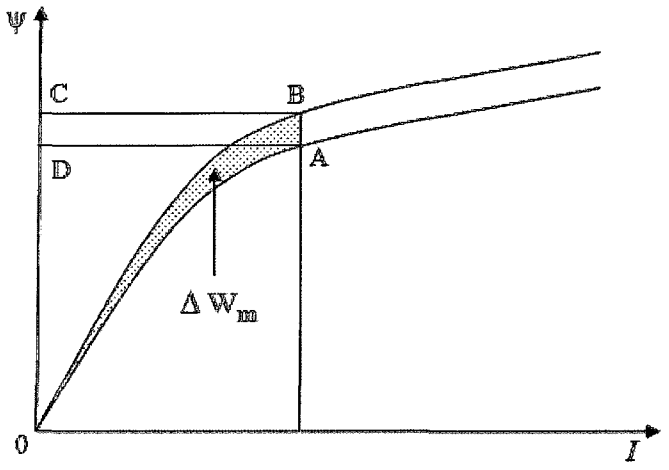

Figure 2.9. Work production for infinitesimal displacement.

If we assume the current to be constant while the rotor is moving from A to B, the incremental mechanical work done is then equal to the change of coenergy, which is actually the complement of the stored field energy. This is explained as during this displacement from A to B, the energy exchange with the supply is equal to the area enclosed by ABCD. The change in stored field energy is:

$$\Delta W_f = OBC - OAD \tag{2.8}$$

and the mechanical work done is:

$$\left.\begin{aligned} \Delta W_m &= T\Delta\theta \\ &= \Delta W_e - \Delta W_f \\ &= ABCD - (OBC - OAD) \\ &= (ABCD + OAD) - OBC \\ &= OAB \end{aligned}\right\} \tag{2.9}$$

From this analysis we realize that the energy supplied from the electric source is partially converted to mechanical work while the rest is stored in the magnetic field and at the end of the stroke is returned to the electric source [58].

From (2.6), (2.7) and if the phase inductance varies linearly with the rotor position for a given current, the torque can then be written as:

$$T = \frac{i^2}{2} \cdot \frac{dL(\theta, i)}{d\theta} \tag{2.11}$$

2.7 Average Torque

To derive the average torque we will study the torque production mechanism, considering the energy conversion theory over a complete stroke from unaligned position of the rotor to fully aligned position. If the motor speed is constant and the rotor is at the unaligned position, the flux-linkage increases according to the equation:

$$\psi = \int (V_s - Ri)dt = \frac{1}{\omega}\int (V_s - Ri)d\theta \tag{2.12}$$

where *Vs*, the voltage source is constant and the winding resistance value is negligible, therefore the flux linkage increases linearly with rotor position. The current initially rises linearly before the rotor enters the overlapping region. But as the poles overlap, the inductance increases and a back-emf builds up which in turn reduces the rise of the current. Fig. 2.11 demonstrates this period of torque production. During this period the two switches (transistor Q1 and Q2 in Fig. 2.14) are conducting. Till this point the electric energy supplied by the voltage source was split into approximately two halves, one was converted to mechanical work depicted in Fig. 2.11 by W_{mt}. and the second half is still stored as field energy in the coil (referred to as W_{fc}). At point C, the two switches turn off and the phase is commutated. The energy that was stored in the field forces the current to flow in the same direction within the coil through the two diodes (D1, D2), therefore the two diodes are forward-biased and hence the voltage applied across the coil terminals is reversed. This is called as the de-fluxing period.

Due to the current that continued to follow after point C, a mechanical work is generated during this de-fluxing period; it is depicted as W_{md} in Fig. 2.12.

As a sum to the complete stroke, Fig. 2.13 shows the whole mechanical work done (W) and the energy returned to the power source (R).

The average torque can now be derived from the number of energy conversion loops (strokes) per revolution and it can be written as follows

$$T = \frac{m \cdot P_r}{2\pi} \cdot W \tag{2.13}$$

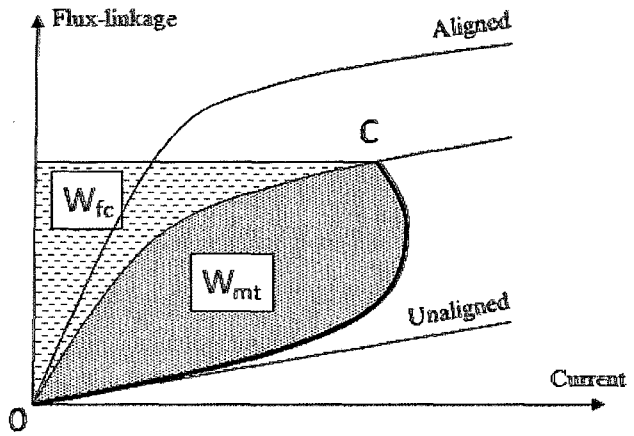

Figure 2.10. Torque production during transistor conduction period.

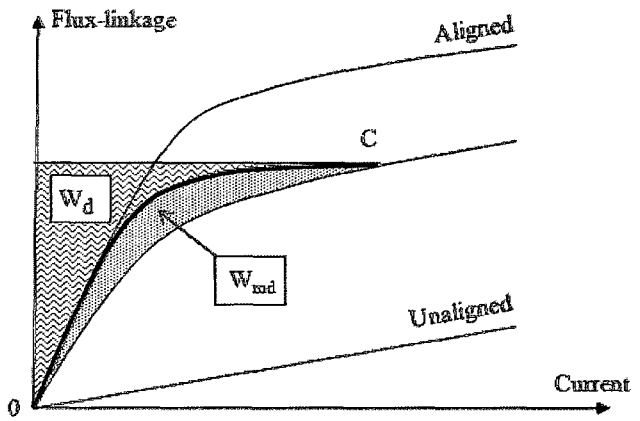

Figure 2.11. Torque production during diode conduction period.

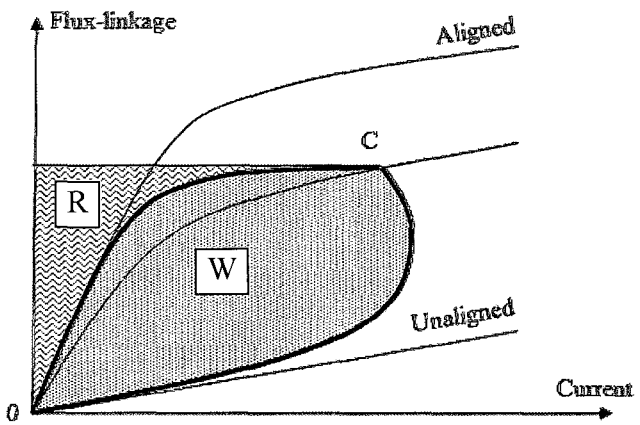

Figure 2.12. Torque production during energy conversion loop.

2.8 Typical Bridge Converter for SRM Drives

Whether it was positive torque (motoring) or negative (regenerative), torque generation in SRMs is independent of current direction, only the phase inductance rate of change that determine which mode of operation it is. Therefore simple drive is sufficient for their operation. The most common SRM converter topology is the one shown in Fig. 2.14. It is for only one phase can be multiplied to match the number of phases required. Note that this asymmetric bridge converter requires 2 power switches and 2 diodes, resembling the conventional ac motor drives. The asymmetric bridge converter offers ease of control, fault tolerance capability and efficiency. To energize phase winding, both transistors Q1 and Q2 are on and the current increases through both switches. If one transistor is off while the other is still on, the winding voltage will be zero. Phase current then slowly decreases by freewheeling through one transistor and one diode (that is called soft switching). When both transistors are off, the phase winding will experience $-V_s$ voltage. Phase current then quickly decreases by freewheeling through the two diodes. The main advantages of this converter are the independent control of each phase and the relatively low voltage rating of the inverter components. The major drawbacks are the total number of switches and a relatively low demagnetizing voltage at high speeds [61].

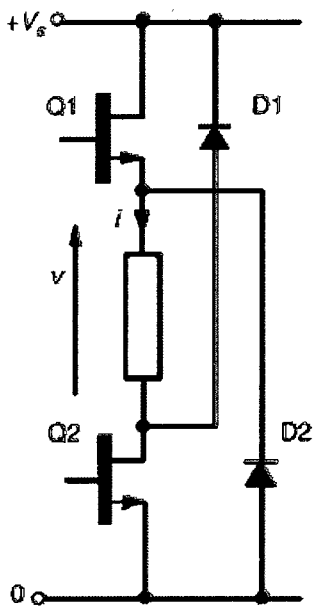

Figure 2.13. Single phase SRM drive.

3 PROPOSED MOTOR

3.1 Proposed Motor Concept and Description

The conceptual diagram for the proposed motor is shown in Fig. 3.2. The stator is composed of 15 c-core, each of which has individually wound coil. The rotor which has a disc shape could be made of any low magnetic permeability material. Through the rotor disc, 12 square holes are created to be filled by 12 cubes of high magnetic permeability material such as iron. The torque production in this design relies on the tendency of any of these cubes (which can be considered as the rotor's poles) to align with the two poles of an energized c-core, providing the minimum reluctance path to the magnetic circuit of one c-core. The motor has 5 phases and 3 repetitions as shown in Fig. 3.1, where the 15 cores on the stator are divided into 3 sets displaced by 120 mechanical degrees for better forces distribution on the structure of the motor.

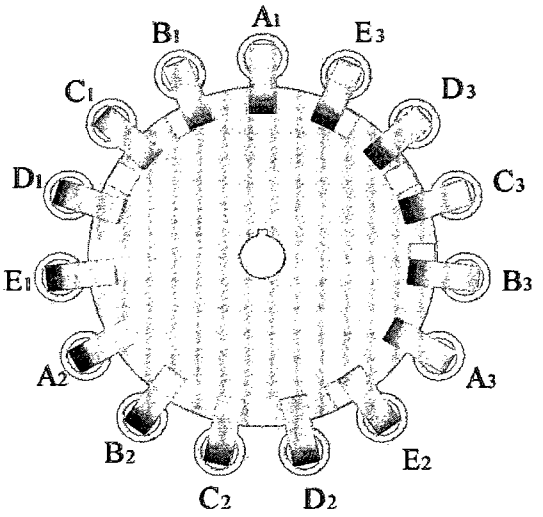

Figure 3.1. Top view of the proposed SRM model with phase distribution.

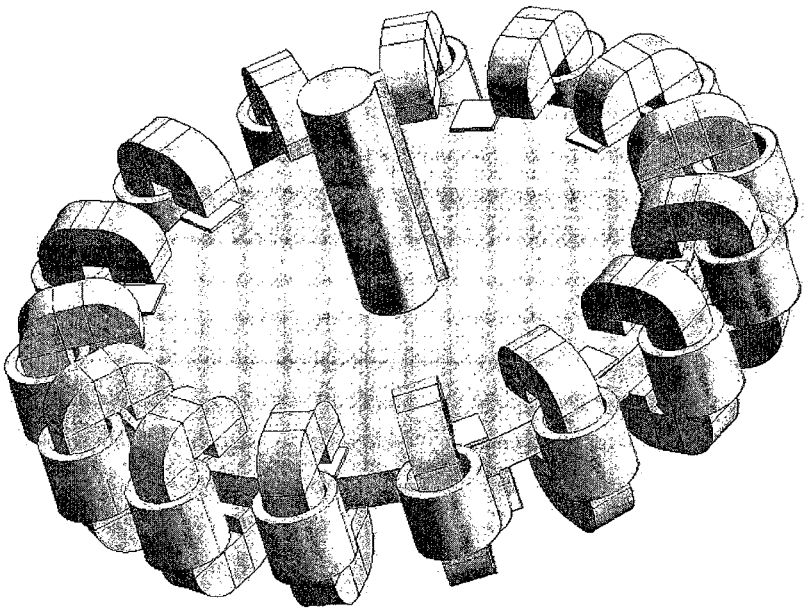

(a)

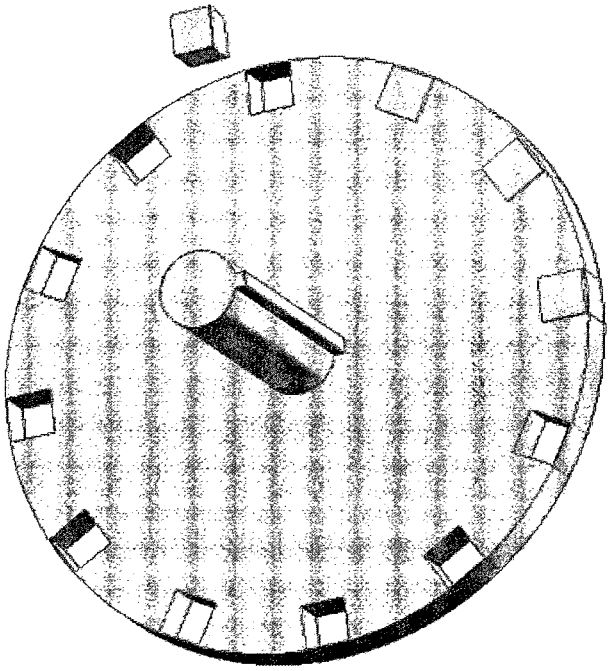

(b)

Figure 3.2. Proposed switched reluctance motor, (a) whole motor, (b) rotor.

3.2 Torque Ripple Reduction

Toque ripple is defined as

$$TR = \frac{T_{Inst_{\max}} - T_{Inst_{\min}}}{T_{Ave}} \tag{3.1}$$

According to [62], the majority of torque ripple occurs in the phase overlap region where the torque producing responsibility is commutated from one energized phase to another. The overlap region is greatly influenced by the step size that is defined as follows

$$\varepsilon = \frac{2\pi}{m \cdot N_r} \tag{3.2}$$

From (3.2) it can be noted that both the number of phases and the number of poles are required to be maximized for the purpose of reducing the torque ripple. However, to adopt high number of phases or poles the diameter of the motor has to be increased which in turn increases the flux path length and hence the losses increase, this is for the case of conventional radial SRM.

In the proposed design, the flux path is independent of the rotor diameter. Therefore, the latter can be increased to allow more space for higher number of poles without affecting the magnetic loading. As a result of having higher number of poles, the step size is reduced which in turn results in minimizing the torque ripple.

3.3 Vibration and Acoustic Noise Minimization

According to literatures [63], [64], the acoustic noise in reluctance motors is mainly generated by the electromagnetic radial force produced by excitation as seen in Fig. 3.3 By peering at the proposed design in Fig. 3.4, it can be seen that the reluctance force developed at the rotor's pole has only tangential components with no radial component produced.; therefore the vibration and the acoustic noise in this design are brought to a low level.

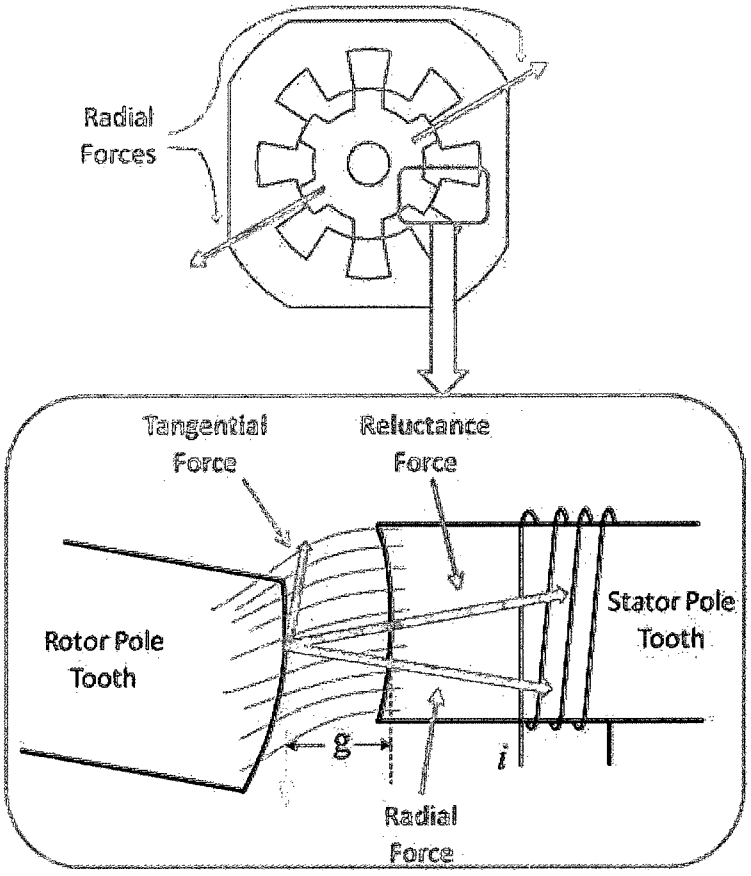

Figure 3.3. Reluctance force components of radial field motor.

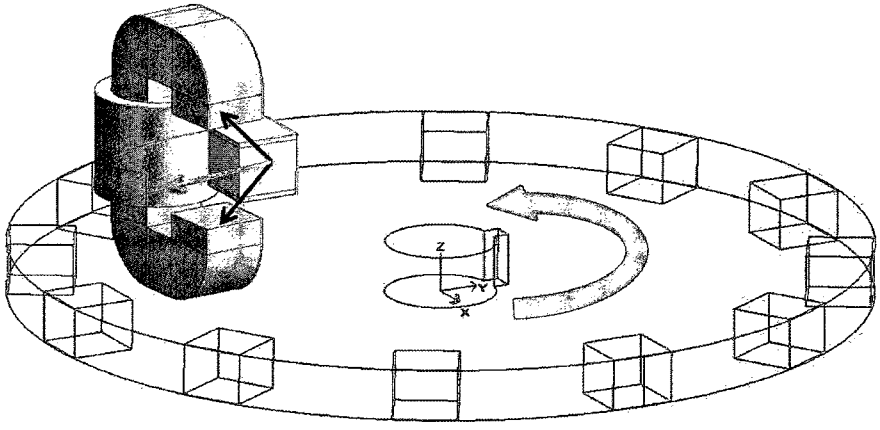

Figure 3.4. Reluctance force component of proposed motor.

3.4 Key Features of the New Design

This design has additional features as compared with typical SRMs, they are summarized as follows:

1. Higher torque and power density:

$$T = \frac{\pi}{4} k_e k_d k_u B A_s D^2 L N_r \tag{3.3}$$

where,

k_e : the efficiency constant.

k_d : the duty cycle constant.

k_u : constant relates the inductance ratio ($K_u = 1 - L_u / L_a^s$)

B, A_s : are the magnetic and electric loading respectively,

D : the bore diameter,

L : the length of motor,

N_r : the rotor speed (rpm).

From (3.3) we see that for a given magnetic and electric loading, the torque is proportional to the square of the diameter. The proposed design has the ability to increase the torque by increasing the diameter of the rotor, without increasing the flux path Length.

2. Larger space available for the coils gives the designer more flexibility in determining the number of turns so the resistance and copper losses are reduced unlike the conventional SRMs that are limited by the slot space. This is illustrated in the specific electric loading formula [60]:

$$A_s = \frac{2N \cdot I \cdot m}{\pi D} \tag{3.4}$$

where, N is the number of turns per phase, I is the current

3. Lower core losses than that in conventional SRM due to the fact that flux reversals do not occur in the stator back iron in addition to having short flux paths.
4. All c-cores are electrically and magnetically isolated from each other so that they can be wound individually without complex winding equipment and by automated process.
5. The inertia of the rotor is small since it can be made of a material that has much lesser mass density than that of the steel which is used in conventional SRM's rotor. In addition, this inertia could be made smaller by creating some openings in the rotor body keeping in mind not to exceed its solidarity limits.
6. Due to its unique pancake shape, this design can be augmented for higher power rating.
7. This design provides a maximized thermal dissipation due to the following:
    - Thin structure of the motor has a better thermal dissipation factor
    - The heat generation source in motors is usually the coils. In this design, they are located on the outer circumference which facilitates a faster and more efficient heat transfer to the outer ambient
    - This special structure also enables it to adopt advanced cooling systems such as water jacket around the motor case.

4 MOTOR DESIGN PROCEDURES

4.1 Geometry Design

The objective of the design is to provide a feasible solution to the well-known drawbacks of SRMs namely the acoustic noise and torque ripple. A considerable work done in the analysis of the acoustic noise suggests that the radial forces account for most of it as mentioned earlier in this thesis. Therefore to meet this constraint, we designed a motor with axial flux so that the magnetic forces are only in the tangential plane to the rotor circumference, thus reducing the radial forces to a very low level.

And regarding the torque ripple, a possible solution according to [58] is to consider higher number of phases so that the number of strokes per revolution increases; as a result the torque dip problem could be alleviated. This solution is not feasible in case of conventional SRM because increasing the number of phases requires larger diameter resulting in a greater flux-path length which in turn raises the losses and reduces efficiency. The solution for this was addressed in this design by adopting a shorter flux-path as shown in Fig. 4.1.

The subsequent step of the design procedure was with the hand calculation of several geometries with varying pole numbers and pole dimensions keeping in mind that several requirements need to be fulfilled such as; minimizing the step size (ε) also known as stroke in some literature, the self starting capability, and the optimum pole arcs.

In this design a small step size of 6 degree was achieved, it was calculated as follows:

$$\varepsilon = \frac{|P_s - P_r|}{P_s \times P_r} \times 360 \text{ Degree} \tag{4.1}$$

where, P_s, P_r are the number of stator poles and rotor poles respectively [65].

To achieve the self stating requirement, the stator arc (β_s) should be greater than the step size (ε). The optimum pole arcs are a compromise between various conflicting

requirements. On the one hand they should be made as large as possible to maximize the aligned inductance and the maximum flux linkage. However, if they are too wide there is not enough clearance between the rotor and stator pole-sides in the unaligned position. This restriction can be represented by:

$$\frac{2\pi}{P_r} - \beta_r \rangle \beta_s \tag{4.2}$$

The optimum pole arcs are somewhere between these extremes. Generally, for very high efficiency designs, the slot area needs to be maximized and this leads to a narrower pole arc [58]. However, in the proposed design this problem does not exist as there is enough space for the windings around the stator cores owing to its unique topology as can be seen from the top view of the motor in Fig. 4.2. Furthermore we can increase this space by extending the c-core length in the radial direction (d_s) adding very negligible magnetic loading to the design. This was actually the case in this design process while trying to achieve the electric and magnetic load balancing. An adequate choice for this design was to have both stator and rotor poles' arcs equal. Fig. 4.3 shows the inductance profile for all phases. It can be noted that the overlap region was increased to offer stronger self-starting capability, large output torque, and little torque ripple. The main parameters and dimensions are presented in table 4.1, and illustrated in Fig. 4.2, and Fig. 4.4.

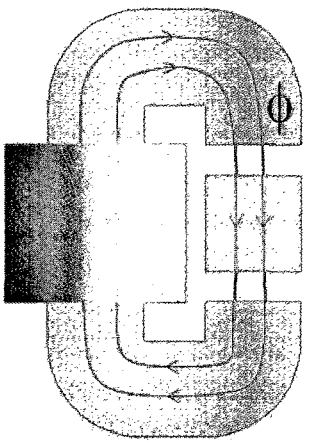

Figure 4.1. Short magnetic flux-path.

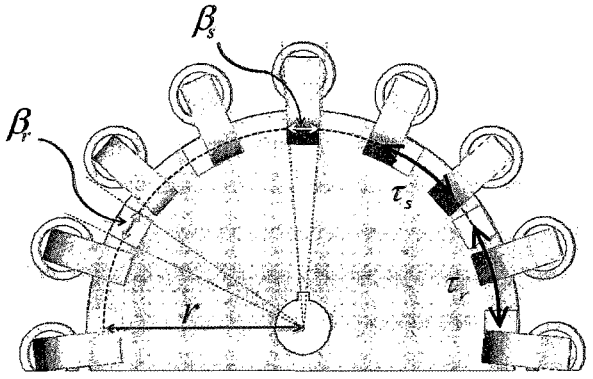

Figure 4.2. Geometry parameters of the proposed SRM.

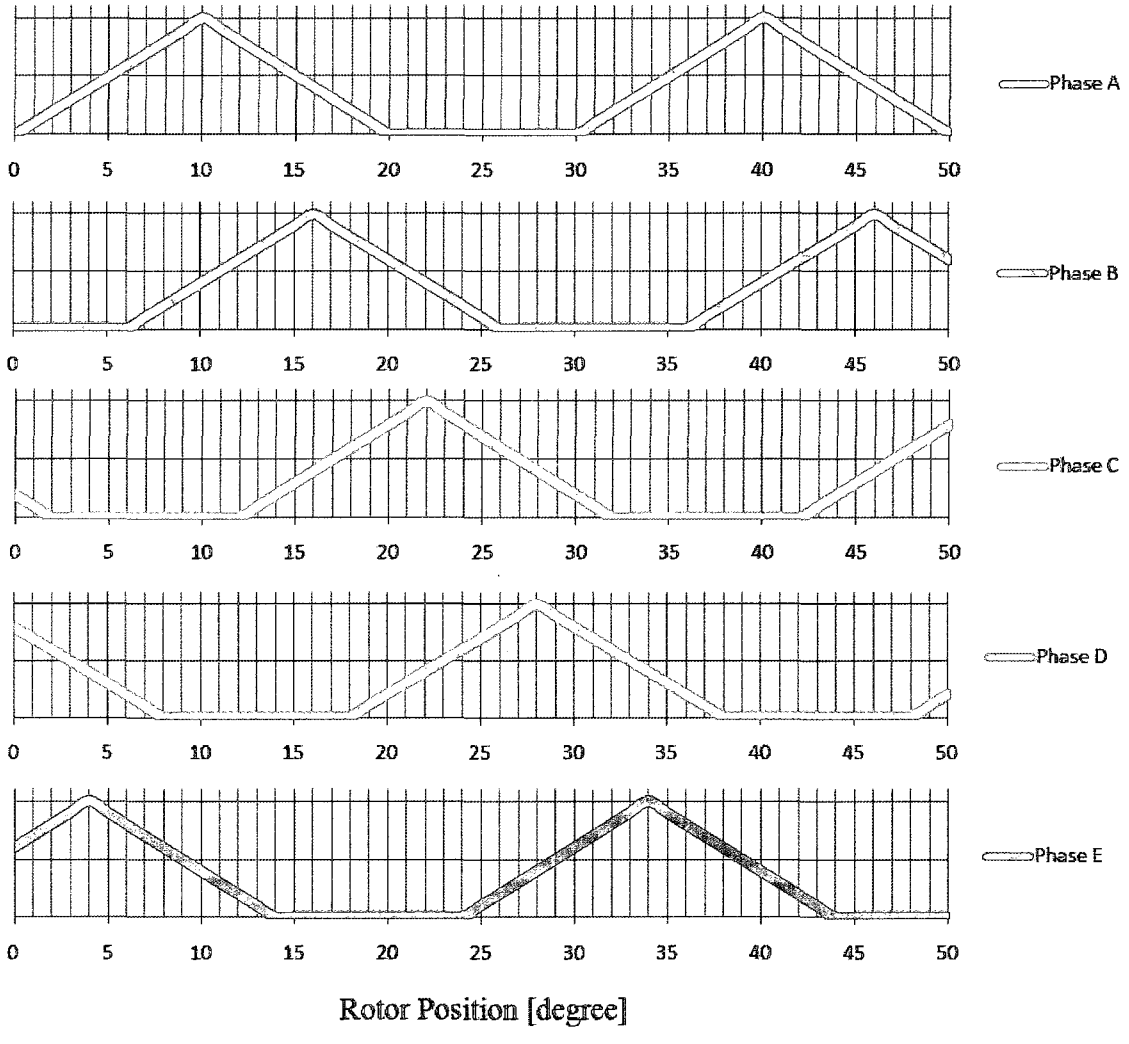

Figure 4.3. Five phases inductance profile.

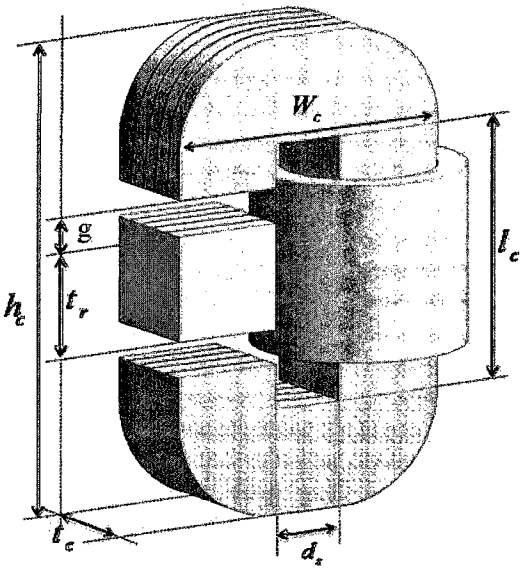

Figure 4.4. C-core dimensions.

Table 4.1. Motor Parameters.

Parameters	Values
The number of phases	5
The stator-rotor configuration	15/12
The rotor pole pitch τ_r	30°
The stator pole pitch t_s	24°
The rotor pole arc β_r	9.6°
The stator pole arc β_s	9.6°
The outer diameter of the rotor D	320 mm
The radius of the centre of a rotor cube r	144 mm
The air gap length g	0.3 mm
The core height h_c	93 mm
The core width W_c	72 mm
The core thickness t_c	24 mm
The rotor thickness t_r	24 mm
The stator pole depth d_s	30 mm
The coil length l_c	45 mm
Number of turns N	40

4.1.1 Material Selection and Orientation

Various materials were studied for the optimization of the motor performance in regard to higher output torque and less losses. The best two options were; M:15-29 and M-19. Both are non-oriented silicon steel have similar lamination thickness of 0.36 mm. The laminations are oriented along the axial plane to suppress eddy current as shown in Fig. 4.4. The B-H characteristics and the loss curves for both materials are presented in Figures 4.5, 4.6, 4.7, and 4.8, for comparison purpose.

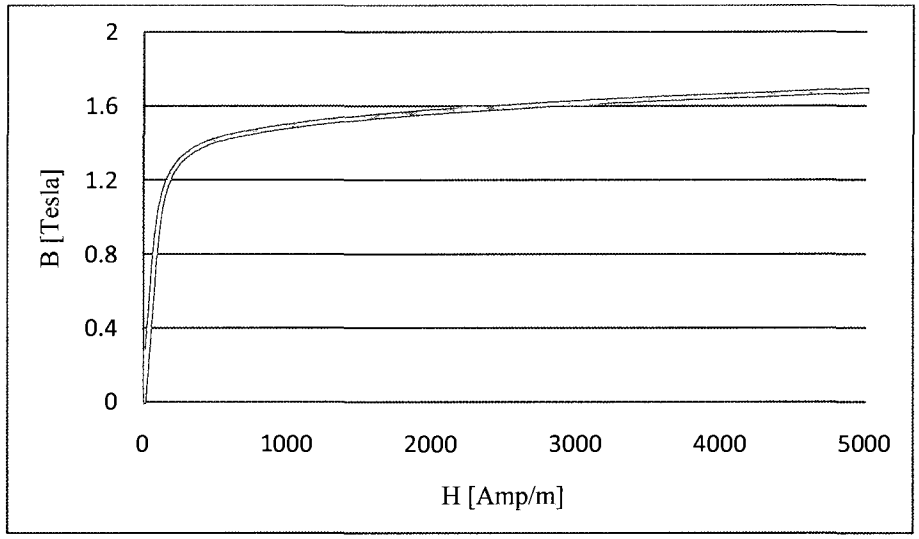

Figure 4.5. B-H characteristics of M-15 29.

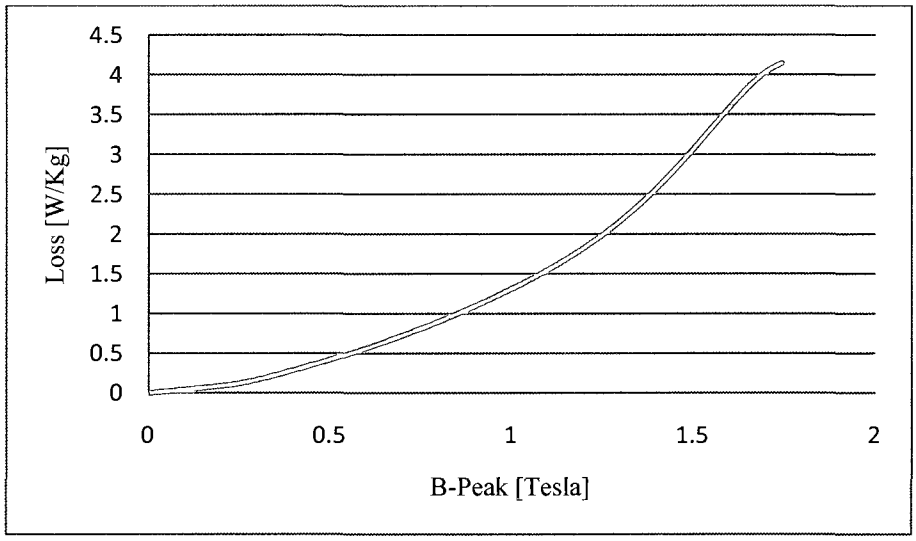

Figure 4.6. Loss-B-Peak characteristics of M-15 29.

M:15-29 shows slightly better characteristics in term of less material loss and higher saturation ratio, therefore it was superior to M-19.

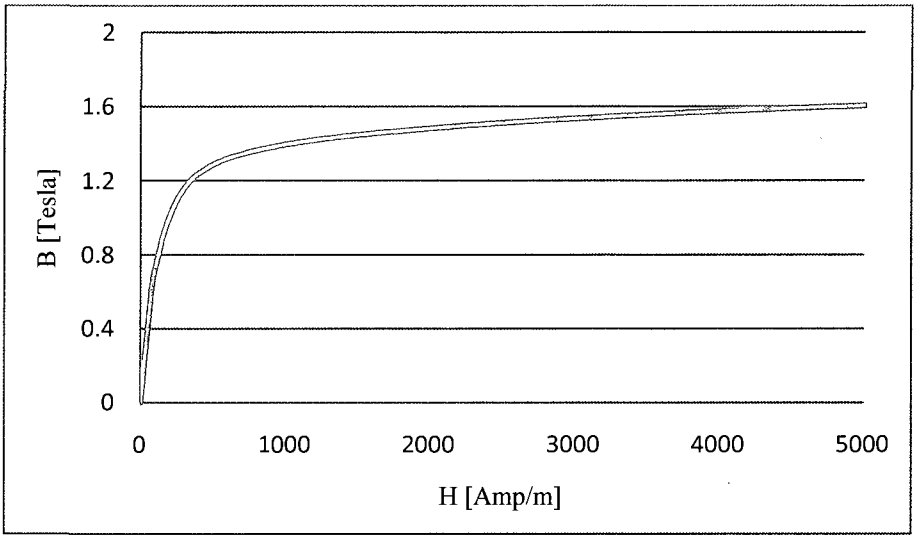

Figure 4.7. B-H characteristics of M -19.

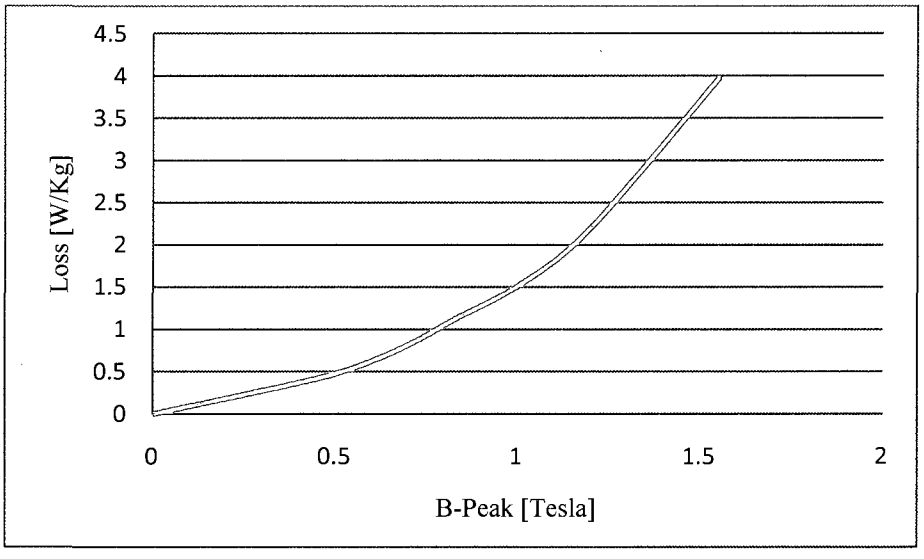

Figure 4.8. Loss-B-Peak characteristics of M-19.

4.2 Analytical Design

4.2.1 Output Power Derivative

Like in AC machines, SRM design starts with deriving the output power equation which is a function of the specific electric loading, magnetic loading, motor speed, and the dimensions of the machine.

The voltage equation for one phase is given by:

$$V = R \cdot I_r + \frac{d(L \cdot I_r)}{dt} \tag{4.3}$$

The current here is assumed to be flat-toped at certain value during the phase conduction period. The phase resistor value is very small so it can be neglected. And the ratio between the aligned and unaligned inductance is known or it can be calculated through an iterative procedure as in [66]. Considering these assumptions, (4.3) can be developed to the following:

$$V = I_r \frac{dL}{dt} \tag{4.4}$$

$$V \cdot t = I_r [L_a - L_u] \tag{4.5}$$

where, L_a is the aligned inductance, L_u is the unaligned inductance.

The time, angular speed of the rotor, and stator arc are related with each other by:

$$t = \frac{\beta_s}{\omega_m} \tag{4.6}$$

The flux-linkage ψ at the aligned position is given by

$$\psi = L_a \cdot I_r = B \cdot A_{sp} \cdot N \tag{4.7}$$

where,

A_{sp}, the stator pole area

N, number of turns per phase

B, is the average flux density. Its value can be obtained from the $B-H$ characteristics of the material used.

The cross section area for the stator pole A_{sp}, is related to the rotor components dimensions as follows:

$$A_{sp} = \beta_s \cdot r \cdot t_r \tag{4.8}$$

where,

β_s, the pole arc of the stator.

r, the radius for the centre point of a rotor cube (rotor pole).

t_r, the rotor-cube line length.

The ratio of the of inductances is termed as:

$$\alpha = \frac{L_a}{L_u} \tag{4.9}$$

Substituting equation (4.6), (4.7), (4.8), and (4.9) in (4.5) gives the voltage equation for the proposed motor:

$$V = \omega \cdot B \cdot r \cdot t_r \cdot N \cdot \left(1 - \frac{1}{\alpha}\right) \tag{4.10}$$

and the phase current can be derived from the specific electric load, equation (3.4)

Finally, the output power can be found from:

$$P_d = k_e \cdot k_d \cdot V \cdot m \cdot I \tag{4.11}$$

4.2.2 Magnetic Circuit Analysis

The most significant inductances in the theory of SRM are the unsaturated aligned inductance L_a^u (this is the slope of the aligned magnetization curve in the linear region) and the unsaturated unaligned inductance L_u. Let σ_u be the unsaturated inductance ratio L_a^u / L_u. Then, since the magnetic circuit has a uniform cross-section, the magnetomotive

force required to produce a maximum flux density of B_s in the stator core is $\sigma_u N i_s$ where, i_s is the current at which the saturation begins [58]. It is the minimum operating current required since it is necessary for SRM to operate within the saturation region to maximize the energy transfer and thus increasing the efficiency.

In the proposed design, the distinction of having completely separated magnetic circuits represented by the c-cores makes it simpler from the designing point of view than the conventional SRM. Considering one c-core along with one rotor cube that completes the magnetic circuit as shown in Fig. 4.1, we can write the required magnetomotive force (MMF) to produce the flux density in the air gap as well as the stator core and the rotor cube, as follows

$$F = F_g + F_c + F_r \tag{4.12}$$

where, F is the total MMF per phase applied and F_g, F_c, and F_r are the MMF drops in the air gap, c-core stator, and rotor cube respectively. In this design, the cross-section and material of the stator and the rotor are identical. Therefore F_c and F_r can be together considered as a part of the circuit, and equation (4.12) can then rewritten as

$$F = Ni = \frac{B_g}{\mu_0} \cdot g + \frac{B_c}{\mu} l_c \tag{4.13}$$

where,

N: number of turns,

B_g: magnetic flux density in the air gap,

B_c: magnetic flux density in the core,

g: air gap length,

l_c: flux path length in the core and rotor cube,

μ: magnetic permeability of the core material,

μ_0: magnetic permeability of the free space.

In the aligned position the phase inductance is at its maximum value because the magnetic reluctance of the flux path is at its lowest. At low current levels, before the saturation starts, most of the reluctance is in the air gap because the magnetic permeability of the core material is much higher than that of the air ($\mu \rangle\rangle \mu_0$). In addition to it, the flux path length in this design is relatively short, as a result, the second term on the right-hand side of equation (4.13) can be neglected and the minimum required current can be determined.

On the other extreme, working in the heavily saturated region is also not recommended as it increases the iron losses which in turn reduce the efficiency. The current at which this occurs will be obtained by utilizing the data from the B-H characteristics of the core material used (M15-29), without neglecting the second term in (4.13) at this time. It was found that the minimum current required is 17 A and the maximum allowable is 275 A. The optimum current can thus be derived on the basis of the maximum increment of co-energy later in this thesis.

In spite of having a completely different structure topology, the new motor has the fundamental torque production mechanism similar to the conventional SRMs. The general expression for the torque produced by one phase at any rotor position is

$$T = \left[\frac{\partial W_{co}}{\partial \theta} \right]_{i=const.} \tag{4.14}$$

where, W_{co} is the coenergy, θ is the angular rotor position. At any position the coenergy is the area below the magnetization curve so it can be defined as follows

$$W_{co} = \int_0^{i_1} \psi di \tag{4.15}$$

where, ψ is the flux linkage at any rotor position as a function of the current.

5 FINITE ELEMENT ANALYSIS AND RESULTS

5.1 Model Formulation

Although the proposed motor is considered as a rotary SRM, it is more like a linear SRM in term of its operation's concept. As mentioned earlier, this design has completely independent magnetic and electric circuits for every c-core; therefore, getting the magnetization characteristics for one case over one stroke range is enough to represent the behavior of the whole motor. Fig. 5.1 shows 3-D model for one c-core along with one iron cube in the fully aligned position.

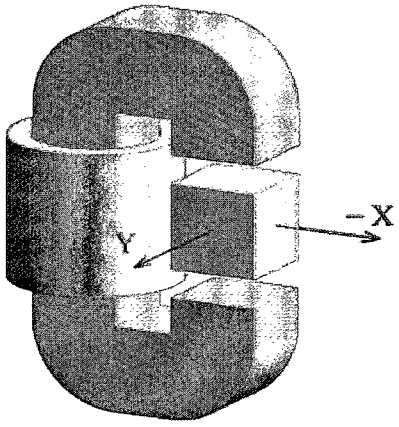

Figure 5.1. 3-D model of one C-core.

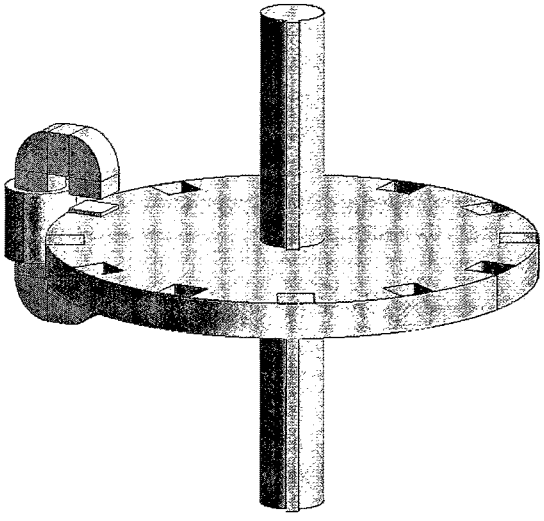

Figure 5.2. 3-D model of one C-core along with the rotor.

During the motor operation, the actual motion of the iron cube is along the Y-axis. So, the flux lines and the motion are in two different planes resulting in a need for a 3-D finite element analysis. As long as our objective is to study the static analysis over short range of displacement (from unaligned to aligned position) and due to its symmetric geometry, the model can be studied and simulated in 2-D analysis by assuming the motion axis to be shifted to the X-coordinate as indicated in Fig. 5.2.

5.2 Finite Element Analysis Results

The modified 2-D model was built using MagNet software. MagNet uses the finite-element method of solving the electromagnetic field equations. This subdivides a 2D model into small triangle elements, forming a mesh that covers the entire region. To improve the solution accuracy, the polynomial order of the elements was chosen to be (3). The mesh was refined by 30%, in which MagNet will select the worst 30% of elements and generate new elements with half their dimensions. Fig. 5.3 shows the meshed 2-D model. Finer mesh elements were generated at the corners and at the areas that require higher accuracy.

5.2.1 Magnetic Flux Solution

The 2-D model was simulated and solved. Fig. 5.4 illustrates the (field solution) finite-element flux-plot when the current was 250 Amps. It can be seen that most of core's regions are saturated. As the rotor moves more toward the full alignment position, the saturation level increases and covers more regions and vice versa. Depending on this plot, the designer can point out the regions that have not been saturated so the material could be saved there.

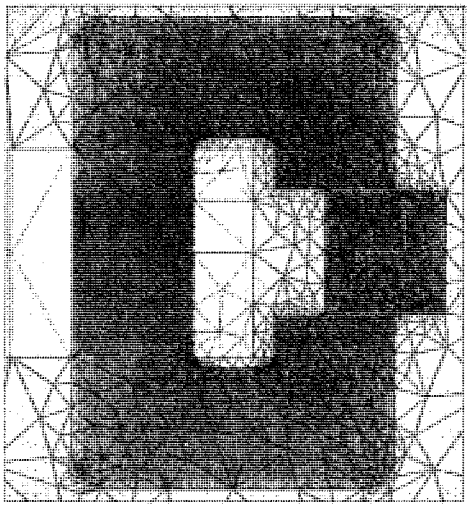

Figure 5.3. FE mesh of C-core model.

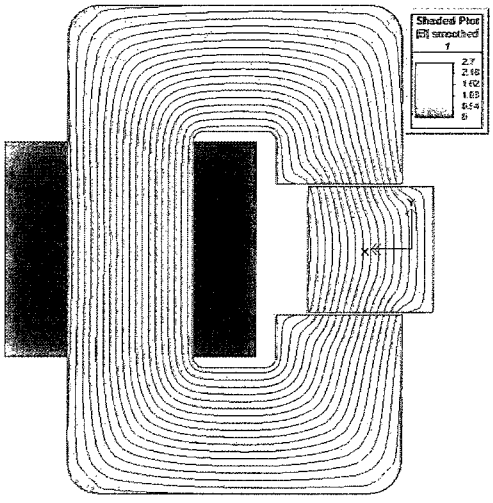

Figure 5.4. Simulated FE magnetic flux plot.

5.2.2 Magnetization Characteristics

The flux-linkage as a function of magnetomotive force (MMF) is shown in Fig. 5.5 for one stroke range, from unaligned to fully aligned position of the rotor. It can be observed in the graph that the curve of the aligned position starts to be saturated at almost 700 (AT) which comes in obvious conformity with the analytical design calculations that had shown a minimum of 17 (A) for the saturation to start (for the aligned rotor position). Similarly, for the maximum allowable current, both analytical and simulation results are

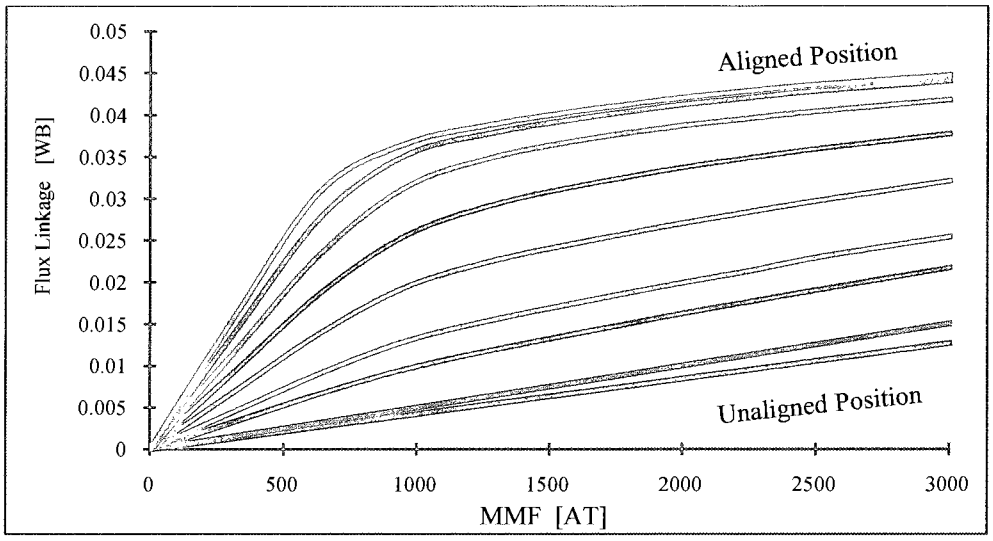

Figure 5.5. The saturation characteristics of the proposed motor (40 turns).

in sufficient agreement that can be inferred from Fig. 5.4. The level of saturation when the current is 250 amp can be read from the color map.

5.2.3 Co-energy and Operating Current

The optimum operating current can be found by referring to equations (4.14) and (4.15) in which was proved that the larger increment of co-energy, the higher increase in the torque.

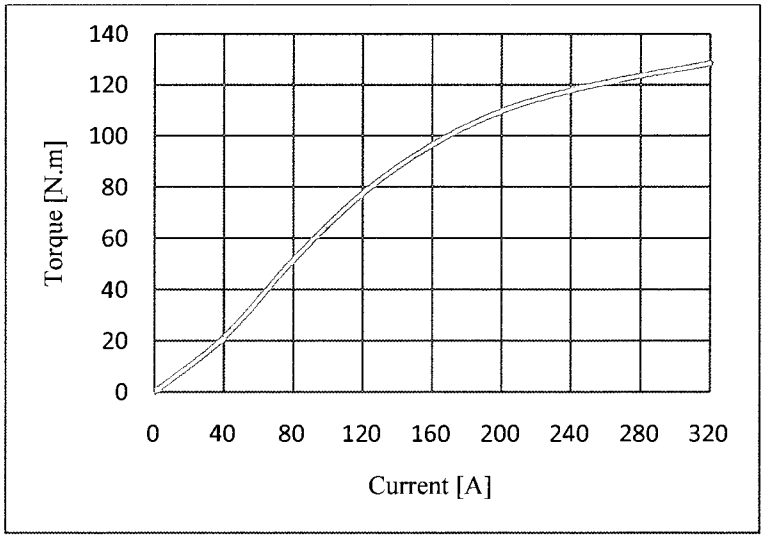

Figure 5.6. Torque current characteristics.

So if we find the current at which the maximum increment of co-energy occurs it would be the optimum operating current. The simulation results for the co-energy increment versus the magnetomotive force are plotted in Fig. 5.7. The plot indicates that 42 ampere is the optimum current. However this result is for the aligned position so it would not be accurate for the for the whole stroke range. As the rotor moves away from alignment, the saturation level decreases and the optimum current is then expected to be higher.

Figure 5.8 shows a set of curves for the torque increment with respect to the current, each of which is at different rotor positions. The curve at 8 degree position which is very close to the complete alignment, points up 50 amps as the optimum current for its position and that assures the latter result in Fig. 5.7. The whole set of curves determine the current range where the motor operates at its higher efficiency to be from 40 till 120 amps. However, the motor can still operate at much higher current ratings to deliver higher torque but with gradually reduced efficiency. The model was simulated at 275 amps to show peak torque value of 123 N.m.

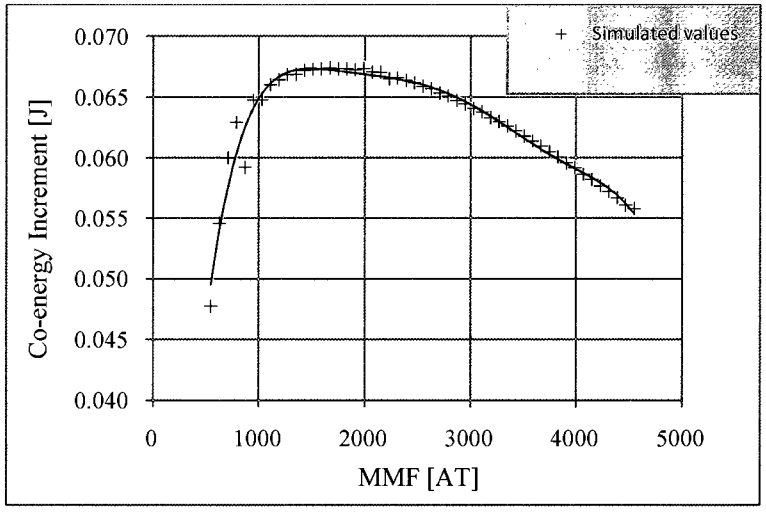

Figure 5.7. Increment of co-energy with respect to magnetomotive force at the aligned position.

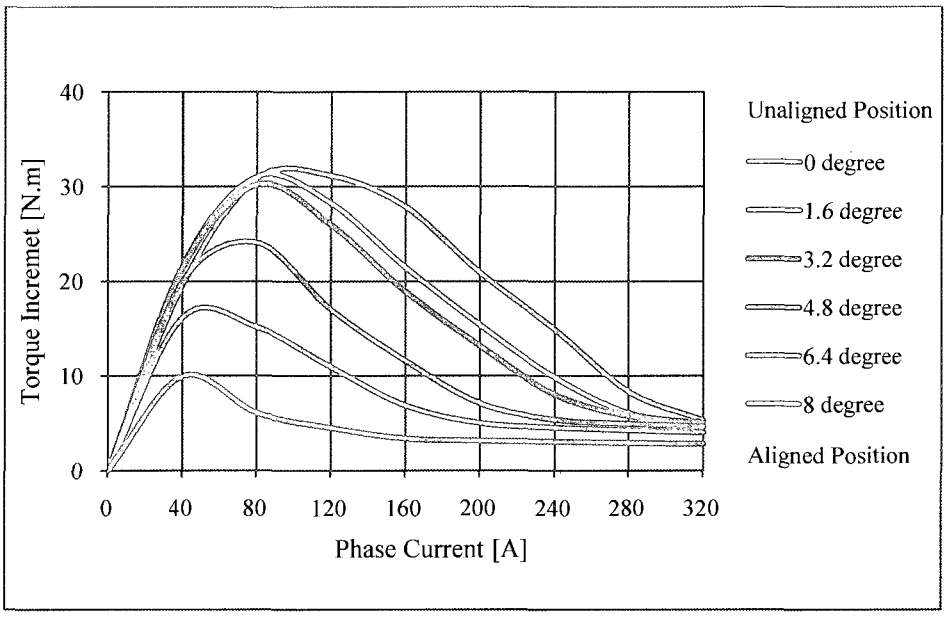

Figure 5.8. Torque increment versus current at different angular positions.

5.2.4 Vibration and Acoustic Noise Reduction

The radial forces on the rotor and stator poles were obtained for aligned position where the radial forces are at their maximum values, different current ratings were applied for this simulation. The simulated results in Fig. 5.9 shows very low values in the range (0 to 3 Newton), which validates the proposed model.

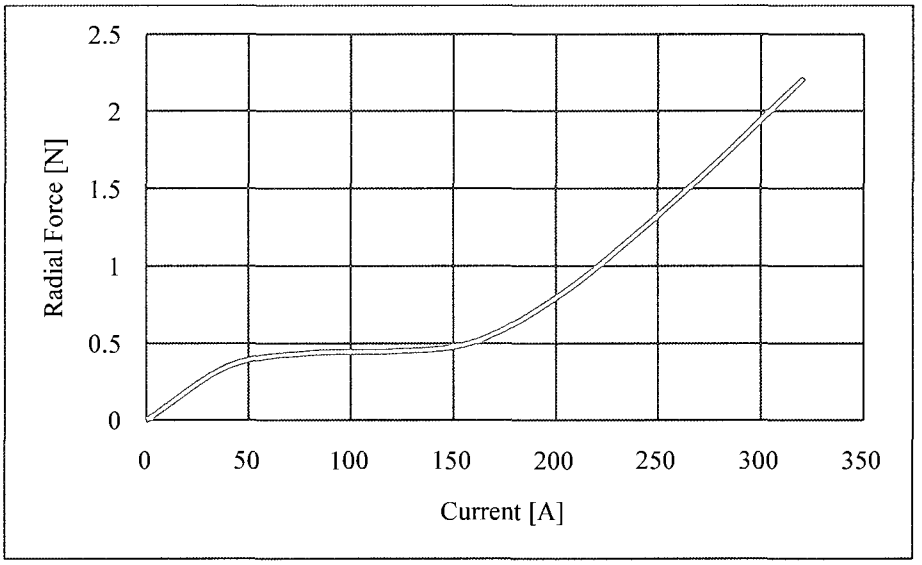

Figure 5.9. Radial force verses current characteristics at aligned position.

5.2.5 Torque Ripple Minimization

Torque ripple is defined as the difference between the maximum and minimum instantaneous torque expressed as a percentage of the average torque during steady state operation [67].

$$TR = \frac{T_{Inst_{\max}} - T_{Inst_{\min}}}{T_{Ave}} \tag{5.1}$$

As per the motor design in [62], the torque ripples have been mitigated to 11% in spite of its complex double layered structure. The new SRM design proposed in this thesis is able to restrain the torque ripples to 8% as shown in Fig.10, without boosting the current in regions of low torque. This result is validated against the design in [62] for a similar output torque range. Their design is shown in Fig. 5.11 and its result is in Fig. 5.12.

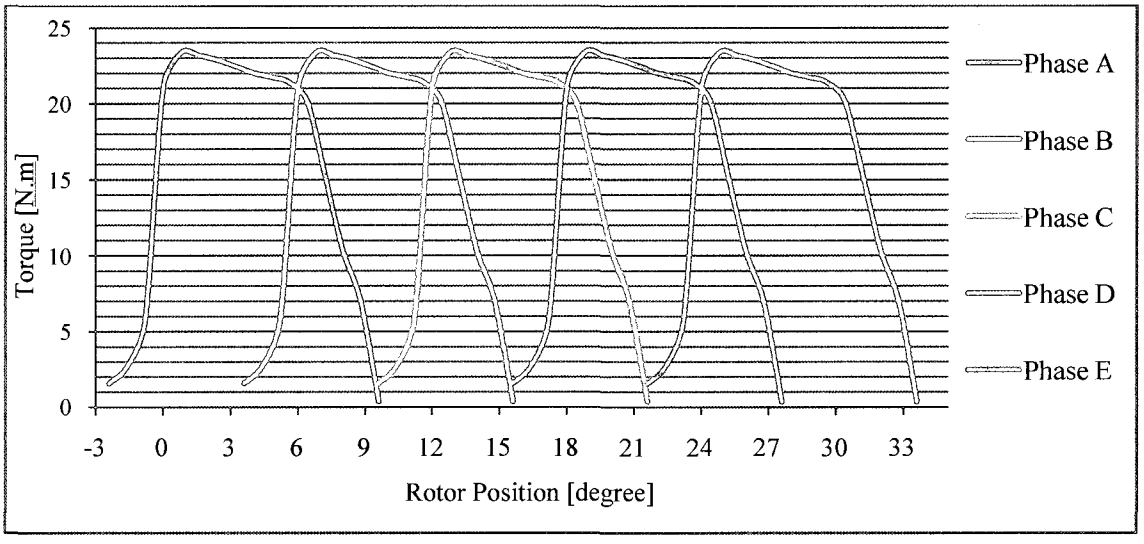

Figure 5.10. Instantaneous torque for the five-phase motor.

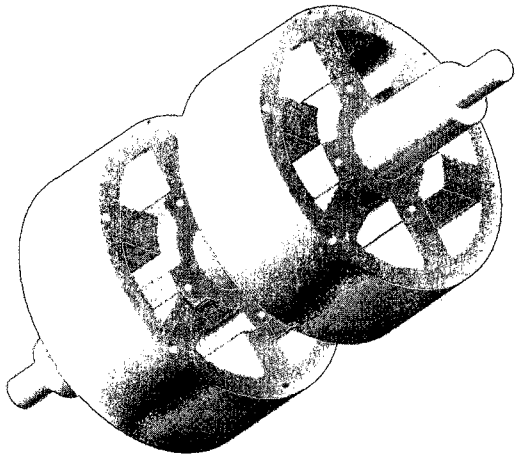

Figure 5.11. Multilayer Switched reluctance motor.

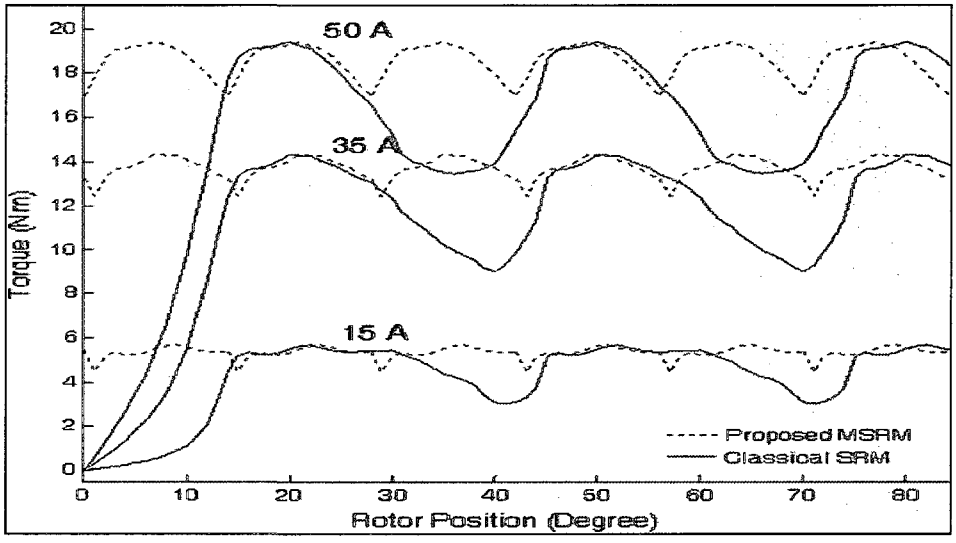

Figure 5.12. Torque ripple for multilayer SRM.

5.2.6 Ohmic Loss Results

Ohmic loss is the power loss in a phase winding due to the resistance of its conductor. It is the product of the square of the current and the resistance of the conductor, described by the formula:

$$P = I^2 \cdot R \tag{5.2}$$

The simulation result in Fig. 5.13 shows the ohmic loss for one coil of a phase.

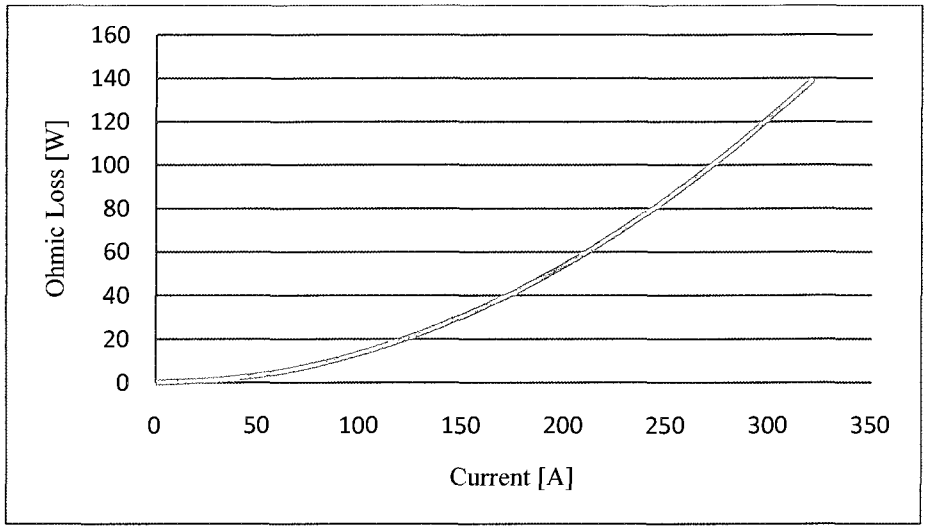

Figure 5.13. Loss-current characteristics for a one coil of a phase.

5.2.7 Machine Characteristics

An iterative design process was employed to reach the final machine's characteristics. By utilizing the magnetization characteristics, the inductance ratio was obtained to be used in the output power equation from chapter four. The machine's characteristics are listed in table 5.1.

Table 5.1. Machine's Characteristics.

Rated Power	20 KW
Rated Phase Voltage	80 V
Rated Phase Current	150 A
Rated Speed	6000 rpm
Maximum Current	275 A
Maximum Power	35 KW

6 MANUFACTURING AND ASSEMBLY

6.1 Manufacturing

In HEV, the motor is subjected to sudden power demands depending upon the driver's need. This sudden demand of power leads to high in rush of current which at times prove harmful to the motors coils. Thus the automotive industry is focused on developing motors that are robust and having economically feasible, easy maintenance for its commercialization. The proposed motor design has a simple and compact assembly without sacrificing its robustness and performance to suit HEV application.

The simple constructional feature reduces the manufacturing constraint of complexity, such as;

- The square cross- sectional geometry allows the use of steel laminations.
- From manufacturing point of view, Steel laminations are better in term of cost and robustness against harsh environment.
- The c-core is to be fitted in the slot that will suppress any harmonic-base vibration among the steel sheets themselves. Consequently, iron loss is reduced.

6.2 Non-Magnetic Components Selection

Selecting of the materials that are not involved in the energy transformation is quite important as most of the losses occur within these components. Alternating magnetic field will induce current that generates heat losses. Solution for this was by searching for a material that is non-magnetic, non-conductive and robust enough to deal with high toque. Kevlar, is found to be one of the best options.

Kevlar is light, strong para-aramid synthetic fiber, related to other aramids such as Nomex and Technora [68]

Developed at DuPont in 1965 by Stephanie Kwolek It was first commercially used in the early 1970s as a replacement for steel in racing tires. Currently, Kevlar has many applications, ranging from bicycle tires to racing sails because of its high strength-to-weight ratio.

General properties of Kevlar:

- Non-magnetic material
- Low Electrical Conductivity
- High Toughness (Work-To-Break)
- Excellent Dimensional Stability
- High Cut Resistance
- High Tensile Strength at Low Weight
- High Chemical Resistance
- Low Thermal Shrinkage

6.3 Assembly

The structural diagram for the motor in Fig. 6.1 gives clear image of how simple the assembly of this design is going to be.

The slots on across which the c-cores are attached restrain it from delocalization in the tangential axis against any kind of vibration. The outer cover prevents delocalization on the radial axis. This design thus permits the motor to maintain a constant air gap in spite of vehicular vibrations. The c-cores are separately wound and located on the outer circumference as shown in the fig. This also reduces the maintenance cost and time as it has the flexibility to replace just the damaged c-core.

Owing to its maximized pole's overlap region, the rotor position sensors might be eliminated which further increase its ease of assembly.

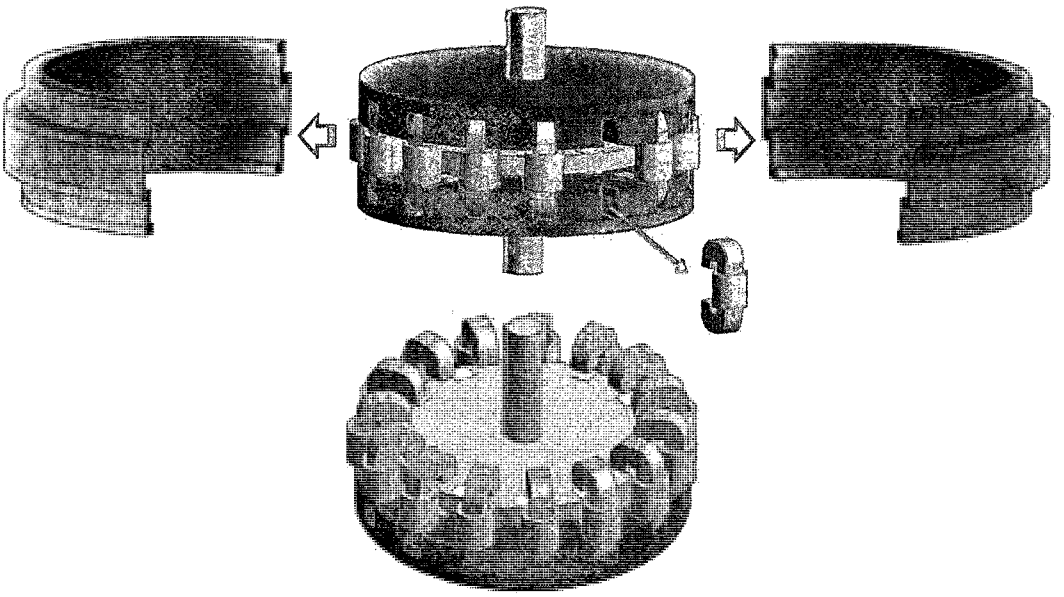

Figure 6.1. Complete structural diagram for proposed model.

7 CONCLUSION AND FUTURE WORK

7.1 Conclusion

In HEV applications SRM can be very successful given that through innovation and design its shortcomings has significantly been conquered as well as its strengths has been amplified. In this thesis a new SRM model has been developed and the developed model has been analyses using FEA simulation software MagNet. The findings of this model are used to analyze its performance and a complete comparative study is performed to validate its abilities. Towards overcoming the shortcoming and enhance the strengths of SRM in HEV application the achievement of this research can be summarized as followings:

- A novel axial field SRM design is proposed which shows a lot of flexibility in all design aspects
- The analysis of the new design demonstrates the improvements in terms of radial forces and torque ripple reduction
- The proposed design shows numerous features which promote it to be a potential candidate for HEV applications
- A simplified and sufficient 2-D FEA model is developed
- Most final motor design aspects and results were obtained by either the analytical method or software simulation method. However, in some steps of the design, results were obtained by both strategies concurrently, as in section 4.2.2, where the operating current range was determined by analytical method and later verified by the magnetization characteristics in section 5.2.2. The comparison shows good agreement between both results.
- The manufacturing issues were addressed to prove its feasibility

7.2 Future Work

In this thesis, the first stage of designing new SRM for HEVs applications has been introduced. An approximate sizing for this design is obtained using the power output equation through an iteration process with the support of finite element analysis software. The static study has produce most of the machine characteristics.

The completion of this project still requires more stages that can be described as follows:

1. To cover all design aspects, the dynamic operation needs to be studied
2. As this design has mainly focused on the analysis of one c-core within 2-D plane, development of the 3-D model could be of great importance to verify the accuracy of the 2-D simplified model results and to analyse the dynamic operation of the design as well
3. Designing the motor drive and control is also recommended to be integrated with this specific motor design
4. And finally, prototyping the new design in order to experimentally validate the simulated results.

REFERENCES

[1] V. Wouk, Hybrid Electric Vehicles, Scientific American, 1997-10, p70-74.

[2] N. Georgano, (2000). Beaulieu Encyclopedia of the Automobile. London: HMSO. ISBN 1-57958-293-1.

[3] B. Rius, (2008). Electric Drive Design for Hybrid Electric Vehicle Optimum Fuel Efficiency. Aachen: Shaker Verlag. ISBN 978-3-8322-7269-2.

[4] C. M. Hogan and A. Gregory, Hybrid vehicle emission noise comparison study, Lumina Technologies, June 1 2006.

[5] C. C. Chan,"The state of the art of electric and hybrid vehicles," Proc. IEEE, vol. 90, no. 2, pp.247-275, Feb. 2002.

[6] M. Zeraoulia, M. E. H. Benbouzid, and D. Diallo, "Electric motor drive selection issues for HEV propulsion systems: A comparative study," *IEEE Trans. on Vehicular Technology*, vol. 55, pp. 1756 – 1764, Nov. 2006.

[7] S. S. Williamson, A. Emadi, and K. Rajashekara, "Comprehensive efficiency modeling of electric traction motor drives for hybrid electric vehicle propulsion applications," *IEEE Trans. on Vehicular Technology*, vol. 56, pp. 1561 - 1572, Part 1, July 2007.

[8] P. Zheng, Y. Liu, Y. Wang, and S. Cheng, "Magnetization analysis of the brushless DC motor used for hybrid electric vehicle," *IEEE Trans. on Magnetics*, vol. 41, pp. 522 - 524, Part 2, Jan. 2005.

[9] P. Zheng, R. Liu, Q. Wu, J. Zhao, and Z. Yao, "Magnetic coupling analysis of four-quadrant transducer used for hybrid electric vehicles," *IEEE Trans. on Magnetics*, vol. 43, pp. 2597 - 2599, June 2007.

[10] J. Malan and M. J. Kamper, "Performance of a hybrid electric vehicle using reluctance synchronous machine technology," *IEEE Trans. on Industry Applications*, vol. 37, pp. 1319 – 1324, Sept.-Oct. 2001.

[11] S. C. Oh and A. Emadi, "Test and simulation of axial flux-motor characteristics for hybrid electric vehicles," *IEEE Trans. on Vehicular Technology*, vol. 53, pp. 912 - 919, May 2004.

[12] I. Boldea, C. I. Pitic, C. Lascu, G. -D. Andreescu, L. Tutelea, F. Blaabjerg, and P. Sandholdt, "DTFC-SVM motion-sensorless control of a PM-assisted reluctance synchronous machine as starter-alternator for hybrid electric vehicles," *IEEE Trans. on Power Electronics*, vol. 21, pp. 711 - 719, May 2006.

[13] I. Boldea, L. Tutelea, and C. I. Pitic, "PM-assisted reluctance synchronous motor/generator (PM-RSM) for mild hybrid vehicles: electromagnetic design," *IEEE Trans. on Industry Applications,* vol. 40, pp. 492 - 498, March-April 2004.

[14] F. J. T. E. Ferreira and A. T. de Almeida, "Novel multi-flux level, three-phase, squirrel-cage induction motor for efficiency and power factor maximization," in *Proc. 2006 IEEE International Conference on Industrial Technology*, pp. 214 – 221.

[15] K. Matsuse, T. Yoshizumi, S. Katsuta, and S. Taniguchi, "High-response flux control of direct-field-oriented induction motor with high efficiency taking core loss into account," , *IEEE Trans. on Industry Applications*, vol. 35, pp. 62 – 69, Jan.-Feb. 1999.

[16] R. E. Janzen and N. C. Kar, "Efficiency improvements from an electric vehicle induction motor drive, with augmentations to a PI control," in *Proc. 2006 Canadian Conference on Electrical and Computer Engineering*, pp. 1228 – 1231.

[17] W. -J. Wang and C. -C. Wang, "Speed and efficiency control of an induction motor with input-output linearization," *IEEE Trans. on Energy Conversion*, vol. 14, pp. 373 - 378, Sept. 1999.

[18] D. de Almeida Souza, W. C. P. de Aragao Filho, and G. C. D. Sousa, "Adaptive fuzzy controller for efficiency optimization of induction motors," *IEEE Trans. on Industrial Electronics*, vol. 54, pp. 2157 - 2164, Aug. 2007.

[19] D. Diallo, M. E. H. Benbouzid, and A. Makouf, "A fault-tolerant control architecture for induction motor drives in automotive applications," *IEEE Trans. on Vehicular Technology*, vol. 53, pp. 1847 - 1855, Nov. 2004.

[20] M. E. H. Benbouzid, D. Diallo, and M. Zeraoulia, "Advanced fault-tolerant control of induction-motor drives for EV/HEV traction applications: From conventional to modern and intelligent control techniques," *IEEE Trans. on Vehicular Technology*, vol. 56, pp. 519 - 528, March 2007.

[21] D. O. Neacsu and K. Rajashekara, "Comparative analysis of torque-controlled IM drives with applications in electric and hybrid vehicles," *IEEE Trans. on Power Electronics*, vol. 16, pp. 240 - 247, March 2001.

[22] S. D. Sudhoff, K. A. Corzine, S. F. Glover, H. J. Hegner and Robey, H.N., Jr., "DC link stabilized field oriented control of electric propulsion systems," *IEEE Trans. on Energy Conversion*, vol. 13, pp. 27 - 33, March 1998.

[23] T. Wang, P. Zheng, Q. Zhang, and S. Cheng, "Design characteristics of the induction motor used for hybrid electric vehicle," *IEEE Trans. on Magnetics*, vol. 41, pp. 505 - 508, Part 2, Jan. 2005.

[24] B. Kou, L. Li, S. Cheng, and F. Meng, " Operating control of efficiently generating induction motor for driving hybrid electric vehicle," IEEE *Trans. on Magnetics*, vol. 41, pp. 488 - 491, Part 2, Jan. 2005.

[25] A. B. Proca, A. Keyhani, and J. M. Miller, "Sensorless sliding-mode control of induction motors using operating condition dependent models," *IEEE Trans. on Energy Conversion*, vol. 18, pp. 205 - 212, June 2003.

[26] K. Asano, S. Okada, and N. Iwamam, "Vibration suppression of induction-motor-driven hybrid vehicle using wheel torque observer," *IEEE Trans. on Industry Applications*, vol. 28, pp. 441 - 447, March-April 1992.

[27] S. Henneberger, U. Pahner, K. Hameyer, and R. Belmans, "Computation of a highly saturated permanent magnet synchronous motor for a hybrid electric vehicle," *IEEE Trans. on Magnetics*, vol. 33, pp. 4086 - 4088, Part 2, Sept. 1997.

[28] F. Crescimbini, A. Di Napoli, L. Solero, and F. Caricchi, "Compact permanent-magnet generator for hybrid vehicle applications," *IEEE Trans. on Industry Applications*, vol. 41, pp. 1168 - 1177, Sept.-Oct. 2005.

[29] J. -M. Kim; S. –K. Sul, "Speed control of interior permanent magnet synchronous motor drive for the flux weakening operation," *IEEE Trans. on Industry Applications*, vol. 33, pp. 43 – 48, Jan.-Feb. 1997.

[30] B. Stumberger, A. Hamler, M. Trlep, and M. Jesenik, "Analysis of interior permanent magnet synchronous motor designed for flux weakening operation," IEEE Trans. on Magnetics, vol. 37, pp. 3644 - 3647, Part 1, Sept. 2001.

[31] D. M. Ionel, J. F. Eastham, T. J. E. Miller, and E. Demeter, "Design considerations for permanent magnet synchronous motors for flux weakening applications," *IEE Proc. on Electric Power Applications*, vol. 145, pp. 435 - 440, Sept. 1998.

[32] M. F. Rahman, L. Zhong, and K. W. Lim, "A direct torque-controlled interior permanent magnet synchronous motor drive incorporating field weakening," *IEEE Trans. on Industry Applications*, vol. 34, pp. 1246 – 1253, Nov.-Dec. 1998.

[33] H. Nakai, H. Ohtani, E. Satoh, and Y. Inaguma, "Development and testing of the torque control for the permanent-magnet synchronous motor," *IEEE Trans. on Industrial Electronics*, vol. 52, pp. 800 - 806, June 2005.

[34] L. Parsa and H. A. Toliyat, "Fault-tolerant interior-permanent-magnet machines for hybrid electric vehicle applications," *IEEE Trans. on Vehicular Technology*, vol. 56, pp. 1546 - 1552, Part 1, July 2007.

[35] F. Caricchi, F. Crescimbini, O. Honorati, G. L. Bianco, and E. Santini, "Performance of coreless-winding axial-flux permanent-magnet generator with power output at 400 Hz, 3000 r/min," *IEEE Trans. on Industry Applications*, vol. 34, pp. 1263 – 1269, Nov.-Dec. 1998.

[36] P. Niazi, H. A. Toliyat, and A. Goodarzi, "Robust maximum torque per ampere (MTPA) control of PM-assisted SynRM for traction applications," *IEEE Trans. on Vehicular Technology*, vol. 56, pp. 1538 - 1545, Part 1, July 2007.

[37] K. -C. Kim, S. -B. Lim, D. -H. Koo, and J. Lee, "The shape design of permanent magnet for permanent magnet synchronous motor considering partial demagnetization," *IEEE Trans. on Magnetics*, vol. 42, pp. 3485 - 3487, Oct. 2006.

[38] M. K.rishnamurthy, C. S. Edrington, A. Emadi, P. Asadi, M. Ehsani, and B. Fahimi, "Making the case for applications of switched reluctance motor technology in automotive products," IEEE Trans. on Power Electronics, vol. 21, pp. 659 - 675, May 2006.

[39] K. M. Rahman, B. Fahimi, G. Suresh, A. V. Rajarathnam, and M. Ehsani, "Advantages of switched reluctance motor applications to EV and HEV: design

and control issues," *IEEE Trans. on Industry Applications*, vol. 36, pp. 111 – 121, Jan.-Feb. 2000.

[40] S. Wang, Q. Zhan, Z. Ma, and L. Zhou, "Implementation of a 50-kW four-phase switched reluctance motor drive system for hybrid electric vehicle," *IEEE Trans. on Magnetics*, vol. 41, pp. 501 - 504, Part 2, Jan. 2005.

[41] C. S. Edrington, M. Krishnamurthy, and B. Fahimi, "Bipolar switched reluctance machines: A novel solution for automotive applications," *IEEE Trans. on Vehicular Technology*, vol. 54, pp. 795 – 808, May 2005.

[42] C. S. Edrington, D. C. Kaluvagunta, J. Joddar, and B. Fahimi, "Investigation of electromagnetic force components in SRM under single and multiphase excitation," IEEE Trans. on Industry Applications, vol. 41, pp. 978 – 988, July-Aug. 2005.

[43] M. Garip, Y. Ozoglu, and E. Mese, "An approach to torque ripple reduction in fully pitched switched reluctance motors by pole tip shaping," in *Proc. 2002 Mediterranean Electrotechnical Conference*, pp. 157 – 161.

[44] D. –H. Lee, Z. –G. Lee, J. Liang, and J. –W. Ahn, "Single-phase SRM drive with torque ripple reduction and power factor correction," *IEEE Trans. on Industry Applications*, vol. 43, pp. 1578 - 1587, Nov.-Dec. 2007.

[45] S. Vukosavic and V. R. Stefanovic, "SRM inverter topologies: a comparative evaluation," IEEE Trans. on Industry Applications, vol. 27, pp. 1034 - 1047, Nov.-Dec. 1991.

[46] G.-J. Su and J. S. Hsu, "A five-leg inverter for driving a traction motor and a compressor motor," *IEEE Trans. on Power Electronics*, vol. 21, pp. 687 – 692, May 2006.

[47] L. A. Tolbert, F. Z. Peng, T. Cunnyngham, and J. N. Chiasson, "Charge balance control schemes for cascade multilevel converter in hybrid electric vehicles," *IEEE Trans. on Industrial Electronics*, vol. 49, pp. 1058 - 1064, Oct. 2002.

[48] T. M. Jahns and V. Blasko, "Recent advances in power electronics technology for industrial and traction machine drives," *Proceedings of the IEEE*, vol. 89, pp. 963 - 975, June 2001.

[49] B. A. Welchko and J. M. Nagashima, "The influence of topology selection on the design of EV/HEV propulsion systems," *IEEE Power Electronics Letters*, vol. 1, pp. 36 - 40, June 2003.

[50] L. Solero, A. Lidozzi, and J. A. Pomilio, "Design of multiple-input power converter for hybrid vehicles," *IEEE Trans. on Power Electronics*, vol. 20, pp. 1007 - 1016, Sept. 2005.

[51] A. Emadi, A. Khaligh, C. H. Rivetta, and G. A. Williamson, "Constant power loads and negative impedance instability in automotive systems: definition, modeling, stability, and control of power electronic converters and motor drives," *IEEE Trans. on Vehicular Technology*, vol. 55, pp. 1112 - 1125, July 2006.

[52] M. Ehsani, K. M. Rahman, M. D. Bellar, and A. J. Severinsky, "Evaluation of soft switching for EV and HEV motor drives," *IEEE Trans. on Industrial Electronics*, vol. 48, pp. 82 - 90, Feb. 2001.

[53] M. Zeroulia, et al, "An investigation of electric motor drive characteristics for EV and HEV propulsion systems," presented at the SAE Technical Paper Series, Paper # 2000-01-3062.

[54] T. J. E. Miller. *Electronic control of switched reluctance machines.* Newnes Publishers, 2001, pp. 1-20

[55] S. A. Nassar. DC switched reluctance motor. *Proceedings IEE*, vol. 116, No 6, 1048-9.

[56] J. V. Byrne and J. G. lacy, Characteristics of saturable stepper and reluctance motor. IEE Conf. Publ. No 136, Small electric machines,93-6, 1976.

[57] P. J. Lawrenson, et al, "Variable-speed switched reluctance motors ," Proceedings IEE vol. 127 Pt B 253-265, 1980.

[58] T. J. E. Miller, *Switched Reluctance Motors and Their Control*, Hillsboro, OH: Magna Physics/Oxford Univ. Press, 1993, pp. 7-60.

[59] Shang-Hsun Mao and Mi-Ching Tsai. "A novel switched reluctance motor with C-core stators," *Magnetics, IEEE Transactions on 41; 41(12)*, pp. 4413-4420.

[60] R. Krishanan, *Switched Reluctance Motor Drives,* CRC Press LLC: Boca Raton, Florida, 2001, p.14.

[61] S. Vukosavic, V. R. Stevanovic, "SRM inverter topologies: a comparative evaluation," *IEEE Transaction on Industry applications*, vol. 27 no. 6 Nov.-Dec. 1991.

[62] F. Daldaban, N. Ustkoyuncu, "Multi-layer switched reluctance motor to reduce torque ripple." *Energy Conversion and Management*, vol. 49, pp. 974–979.

[63] N. Sadowski, Y. Lefevre, C. G. Neves, and R. Carlson, "Finite element coupled to electrical circuit equations in the simulation of switched reluctance drives," *IEEE Trans. on Mag.,* vol. 32, No. 3, pp. 1086-1089, 1993.

[64] C. Liu, J. Kuo, L. Chen, Y. Lee, C. Leu, and Y. Chen, "Interaction force analysis of transverse flux linear switched reluctance machine by fourier projection," *IEEE Trans. on Energy Conv..,* vol. 11, pp. 62-69, 1996.

[65] L. E. Unnewehr, "Stepper motors" in *Handbook of electric motors,* New York: Marcel Dekker Inc., 1995.

[66] R. Krishnan and P. Materu, "Analytical prediction of SRM inductance profile and steady state average torque," Accepted for Presentation In IEEE IAS Annual Meeting, Seattle, Oct, 1990.

[67] I. Husain, "Minimization of torque ripple in SRM drives," *IEEE Trans Ind. Electronics*, 2002;49(1):28–39.

[68] Dopont Kevlar® webpage, "Kevlar® products technical information" Internet: http://www2.dupont.com/Kevlar/en_US/tech_info/index.html, [Sep. 21, 2009]

LIST OF PUBLICATIONS

[1] A. Labak and N. Kar, "A Novel Five-Phase Pancake Shaped Switched Reluctance Motor for Hybrid Electric Vehicles," IEEE VPPC Conference, September, 2009.

VITA AUCTORIS

Name	Anas Labak
Place of Birth	Aleppo, Syria
Year of Birth	1971
Education	*University of Windsor, Windsor, Ontario* *2007-2009* *M.A.Sc.* *University of Aleppo, Syria* *1990-1996* *B.A.Sc.*